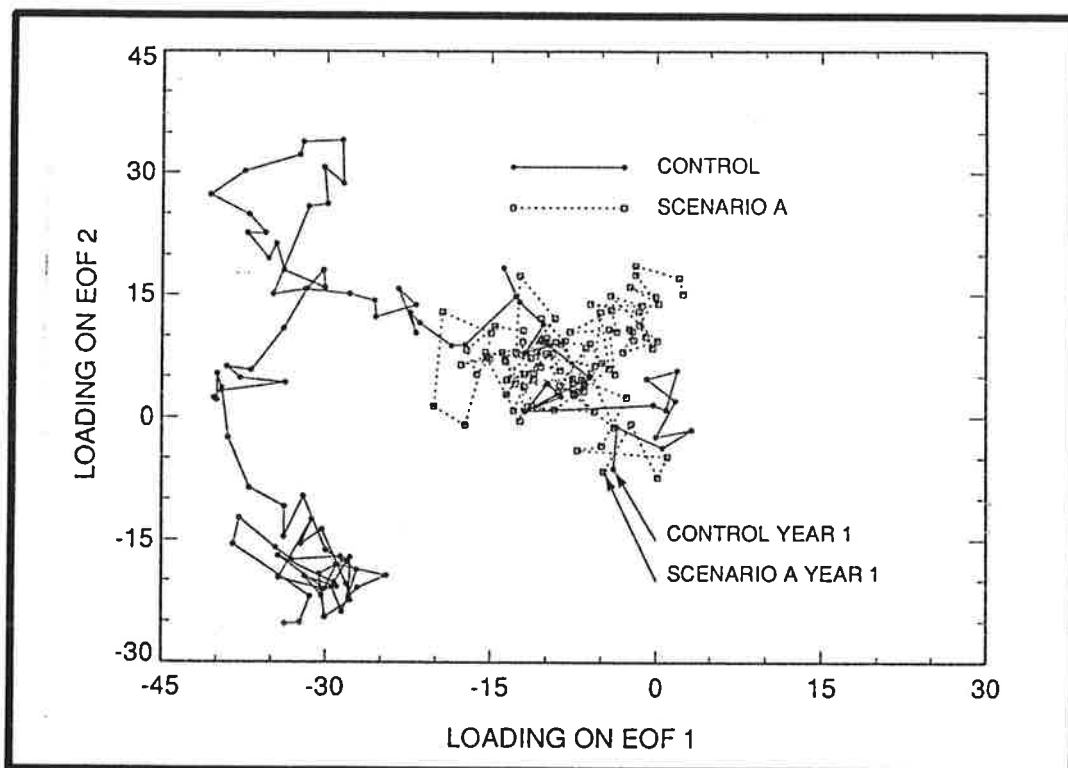




# Max-Planck-Institut für Meteorologie

## REPORT No. 98



### SIGNAL-TO-NOISE ANALYSIS OF TIME-DEPENDENT GREENHOUSE WARMING EXPERIMENTS. PART 1: PATTERN ANALYSIS

by

BENJAMIN D. SANTER • WOLFGANG BRÜGGEMANN • ULRICH CUBASCH  
KLAUS HASSELMANN • HEINKE HÖCK • ERNST MAIER-REIMER • UWE MIKOLAJEWICZ

HAMBURG, JANUARY 1993

AUTHORS:

Wolfgang Brüggemann  
Ulrich Cubasch  
Klaus Hasselmann  
Heinke Höck  
Ernst Maier-Reimer  
Uwe Mikolajewicz

Max-Planck-Institut  
für Meteorologie

Benjamin D. Santer

Program for Climate  
Model Diagnosis and Intercomparison  
Lawrence Livermore National Laboratory  
P.O. Box 808, Mail-Stop L-264  
Livermore  
CA 94550  
U.S.A.

MAX-PLANCK-INSTITUT  
FÜR METEOROLOGIE  
BUNDESSTRASSE 55  
D-2000 HAMBURG 13  
F.R. GERMANY

Tel.: +49 (40) 4 11 73-0  
Telex: 211092 mpime d  
Telemail: MPI.METEOROLOGY  
Telefax: +49 (40) 4 11 73-298

# Signal-to-Noise Analysis of Time-Dependent Greenhouse Warming Experiments. Part 1: Pattern Analysis

Benjamin D. Santer<sup>1</sup>, Wolfgang Brüggemann<sup>2</sup>, Ulrich Cubasch<sup>2</sup>, Klaus Hasselmann<sup>2</sup>, Heinke Höck<sup>2</sup>, Ernst Maier-Reimer<sup>2</sup>, and Uwe Mikolajewicz<sup>2</sup>

<sup>1</sup> Program for Climate Model Diagnosis and Intercomparison, Lawrence Livermore National Laboratory, Livermore, CA 94550

<sup>2</sup> Max-Planck-Institut für Meteorologie, Bundesstrasse 55, 2 Hamburg 13, Germany

17 December, 1992

## Abstract

Results from a control integration and time-dependent greenhouse warming experiments performed with a coupled ocean-atmosphere model are analysed in terms of their signal-to-noise properties. The aim is to illustrate techniques for efficient description of the space-time evolution of signals and noise and to identify potentially useful components of a multivariate greenhouse-gas “fingerprint”. The three 100-year experiments analysed here simulate the response of the climate system to a step-function doubling of  $\text{CO}_2$  and to the time-dependent greenhouse-gas increases specified in Scenarios A (“Business as Usual”) and D (“Draconian Measures”) of the Intergovernmental Panel on Climate Change (IPCC).

If signal and noise patterns are highly similar, the separation of the signal from the natural variability noise is difficult. We use the pattern correlation between the dominant EOFs of the control run and the Scenario A experiment as a measure of the similarity of signal and noise patterns. The EOF 1 patterns of signal and noise are least similar for 2m temperature and the vertical structure of zonal winds, and are most similar for sea level pressure (SLP). The dominant signal and noise modes of precipitable water and stratospheric/tropospheric temperature contrasts show considerable pattern similarity. Despite the differences in forcing history, a highly similar EOF 1 surface temperature response pattern is found in all three greenhouse warming experiments. A large part of this similarity is due to a common land-sea contrast component of the signal.

To determine the degree to which the signal is contaminated by the natural variability (and/or drift) of the control run, we project the Scenario A data onto EOFs 1 and 2 of the control. Signal contamination by the EOF 1 and 2 modes of the noise is lowest for 2m temperature, a situation favorable for detection. The signals for precipitable water, SLP, and the vertical structure of zonal temperature and zonal winds are significantly contaminated by the dominant noise modes.

We use cumulative explained spatial variance, principal component time series, and projections onto EOFs in order to investigate the time evolution of the dominant signal and noise modes. In the case of 2m temperature, a single pattern emerges as the dominant signal component in the second half of the Scenario A experiment. The projections onto EOFs 1 and 2 of the control run indicate that Scenario D has a large common variability and/or drift component with the control run. This common component is also apparent between years 30-50 of the Scenario A experiment, but is small in the  $2\times\text{CO}_2$  integration. The trajectories of the dominant Scenario A and control run modes evolve differently, regardless of the basis vectors chosen for projection, thus making it feasible to separate signal and noise within the first two decades of the experiments. For Scenario D it may not be possible to discriminate between the dominant signal and noise modes until the final 2-3 decades of the 100-year integration.

# 1 Introduction

In the past five years, several modeling groups have performed numerical experiments with coupled ocean-atmosphere general circulation models (GCMs) in order to investigate the response of the climate system to time-dependent increases in greenhouse gases (Stouffer et al., 1989; Washington and Meehl, 1989; Manabe et al., 1991; Cubasch et al., 1992). Such experiments typically yield information on the time evolution of many hundreds of climate variables on three-dimensional spatial grids in the atmosphere and ocean. The greenhouse signal one wishes to investigate is superimposed on the broad-band natural variability of the coupled ocean-atmosphere system. To analyse the enormous volumes of data produced in such integrations, it is thus necessary to develop efficient methods of describing the space-time evolution of both the climate signal in the response experiment and the internally-generated ‘noise’ of the coupled ocean-atmosphere system in a control run with no greenhouse-gas forcing.

Appropriate statistical techniques are also needed to establish the signal-to-noise (S/N) properties of the different fields (Wigley and Barnett, 1990). The standard method for detecting a predicted greenhouse signal in observed data is to compare the observed changes in a climate variable, such as surface temperature (e.g. Wigley and Jones, 1981; Barnett, 1986; Barnett and Schlesinger, 1987; Santer et al., 1991, 1992) or troposphere/stratosphere temperature contrast (Károly, 1987, 1989) with the changes predicted by a climate model in response to greenhouse-gas forcing. Before performing such comparisons, however, it is important to identify those climate variables and spatial scales which are optimal for detection purposes. By limiting the comparison of model and real-world climate changes to a subset of variables with favorable signal-to-noise properties, the chances of detecting an enhanced greenhouse effect signal in the observed data are improved. The use of a signal comprised of a number of different variables – a so-called multivariate “fingerprint” – also increases the chances of unambiguously attributing a change in climate to the enhanced greenhouse effect (Madden and Ramanathan, 1980; MacCracken and Moses, 1982; Hasselmann, 1993).

In previous greenhouse-gas experiments, at least three general aspects of signal-to-noise behavior have been investigated:

1. Overall magnitude: some measure of the overall change in mean (response minus control) relative to the temporal variance of the control or the (pooled) variance of control and response (Wigley and Jones, 1981; Barnett and Schlesinger, 1987; Barnett et al., 1991; Santer et al., 1991).
2. Orthogonality properties: the similarity of signal and noise spatial patterns (Barnett and Schlesinger, 1987; Barnett et al., 1991; Mikolajewicz et al., 1992).

3. Significance of trend: the relationship between the magnitude of a trend in a time-evolving signal and the variance of trends (on the time scale appropriate to the signal) in a long control run (Mikolajewicz et al., 1992).

Previous studies have dealt almost exclusively with signal-to-noise properties in equilibrium response experiments with step-function doubling of CO<sub>2</sub>, and thus have focussed on (1) and (2). As more time-dependent greenhouse-gas experiments are performed, it will become increasingly important to consider (3) and explicitly include the time dimension in estimating signal-to-noise properties. The problem is to determine whether the trend in a time-dependent response experiment is large relative to the ‘unforced’ trends (on time scales of 100 years and longer) which could occur solely due to internally-generated variability of the coupled ocean-atmosphere system. This issue is considered in Part 2 of this paper (Santer et al., 1993).

As a basis for this second study, we examine here the pattern signal-to-noise properties of a control run and three time-dependent greenhouse warming experiments recently performed with a coupled ocean-atmosphere model (Cubasch et al., 1992). The aim is to illustrate techniques for efficient description of the space-time evolution of signal and noise, and to identify potentially useful components of a greenhouse-gas “fingerprint”.

## 2 Model and Experiments

The model used for the time-dependent integrations analysed below consists of an atmospheric GCM (ECHAM-1) coupled to a large scale geostrophic ocean GCM (LSG). ECHAM-1 is a low resolution (T21; 19 vertical layers) version of the spectral forecast model developed at the European Centre for Medium Range Weather Forecasts (ECMWF). It has been extensively modified for climate purposes in Hamburg (Roeckner et al., 1989), and has been used for a number of different sensitivity experiments (Cess et al., 1989; Lautenschlager and Herterich, 1990).

The LSG ocean GCM developed by Maier-Reimer and Hasselmann (1987) is based on a numerical formulation of the primitive equations appropriate for large scale geostrophic motion. It has 11 vertical levels and a horizontal resolution of 3.5° x 3.5°. A detailed description of the model physics and control run performance is given by Maier-Reimer et al. (1993). The LSG model has been used in paleoclimate studies (Maier-Reimer and Mikolajewicz, 1989), a stochastic forcing experiment (Mikolajewicz and Maier-Reimer, 1990) and to investigate the ocean response to greenhouse warming (Mikolajewicz et al., 1990).

A full description of the coupling procedure and flux correction scheme (Sausen et al.,

1988) is given in Cubasch et al. (1992), together with information on the fidelity with which the coupled model reproduces important features of the observed climate.

Four numerical experiments were carried out with the coupled model. The recent report of Working Group 1 of the Intergovernmental Panel on Climate Change (IPCC; Houghton et al., 1990) presented four scenarios of future changes in greenhouse-gas concentrations, ranging from unrestricted emissions in Scenario A (“Business as Usual”) to severe restriction of greenhouse-gas emissions after the year 2000 in Scenario D (“Draconian Measures”). These scenarios were used to force the coupled model in two separate 100-year experiments. In a third greenhouse warming experiment, the response of the coupled model to an instantaneous doubling of equivalent atmospheric CO<sub>2</sub> concentration was considered. For reference, a 100-year control run was performed with fixed equivalent CO<sub>2</sub> concentration.

A full description of the design of the control run and greenhouse warming experiments is given in Cubasch et al. (1992), together with a brief analysis of the evolution of the surface air temperature signal. Here, the space-time evolution of the surface air temperature signal and noise is considered in more detail.

## 3 Time Evolution of Surface Air Temperature

### 3.1 The Control Run

The global mean annually-averaged near surface air temperature of the control run drifts by less than 0.4° K during the 100-year integration. However, this quasi-stationarity with respect to the global mean masks relatively large positive and negative changes in the spatial distribution of temperature, with high latitude cooling in the Northern Hemisphere and warming in the Southern Hemisphere (Figure 1). These changes are coherent in time and space. The spatial pattern of temperature change in the final decade of the control run (relative to the initial state of the control run) is characterized by strong cooling ( $\approx 5^\circ\text{C}$ ) in the Arctic and warming in the Ross Sea ( $\approx 6^\circ\text{C}$ ) and Weddell Sea ( $\approx 4^\circ\text{C}$ ) (Figure 2a). The area-weighted r.m.s. of this anomaly field is 1.1° C.

An important question is whether these changes represent internally-generated natural variability of the coupled ocean-atmosphere system, spurious drift, or some combination of both. Unfortunately, it is very difficult to discriminate between drift and natural variability without performing significantly longer integrations ( $\geq 500$  years) with the coupled model. Such experiments have not yet been conducted. Although we cannot, therefore, definitively answer the question of whether the control run changes are due to natural variability or drift, we briefly examine the evidence for each interpretation.

Some evidence for a natural variability interpretation is provided by the results of a 3,800-year integration with the LSG ocean model (Mikolajewicz and Maier-Reimer, 1990), in which the ocean was forced by temporally white, spatially-correlated variations in fresh water fluxes representative of natural weather variability. This uncoupled experiment yielded typically red variance spectra for a variety of ocean circulation indices (e.g. heat transport, streamfunction, ice volume, etc.), with spectral variance increasing towards low frequencies for time scales up to several centuries. The variability displayed by the coupled model is consistent with these results. There is also some agreement in the spatial pattern of variability: both coupled and uncoupled experiments showed large variability in the vicinity of the Antarctic Circumpolar Current, a relatively sensitive region of the ocean circulation. However, in view of the idealized nature of the uncoupled experiment (the feedback loop through the atmosphere was not included), we cannot compare the pattern structures in detail.

On the other hand, a comparison of the spatial patterns of the control run anomalies (Figure 2a) and the flux correction fields (not shown) suggests a drift interpretation of the control run non-stationarity. There is close agreement between the location of the large, positive SST anomalies in the Ross and Weddell Seas in the control run and the location of the largest heat flux corrections (which is known to have problems particularly near sea-ice boundaries). This indicates that some of the non-stationarity in control run SST may be attributable to incomplete drift compensation by the flux correction, at least at high latitudes in the Southern Hemisphere. In the Northern Hemisphere, however, the alternating warm and cool episodes (Figure 1) are difficult to explain by drift alone, since flux correction errors would presumably induce a constant drift.

In the presence of substantial climate drift and/or natural variability, the evolution of the signal and its S/N properties can be sensitive to the way in which the signal is defined. Here, as in Cubasch et al. (1992), we regard the non-stationarity of the control run as inherent natural variability of the coupled model. Assuming that the natural variability in the control run and the response experiments are uncorrelated, we define the time-dependent climate response in all three greenhouse warming simulations as the deviation with respect to the average of the first 10 years of the control run (Definition 1). This is the preferred definition used in the following. We also consider an alternative definition based on the assumption that the control run changes represent a spurious drift or component of natural variability that is common to the control and response integrations. In this case it is more appropriate to subtract this common component and define the climate signal as the instantaneous difference between response experiment and control (Definition 2).

## 3.2 The Response Experiments

The global, annually-averaged changes in surface air temperature in the three response experiments have been described in Cubasch et al. (1992). The most important features to note are the initial slow temperature increase in Scenario A over the first 40 years ( $0.12^{\circ}\text{C}/\text{decade}$ ), followed by a more rapid, approximately linear increase of  $0.35^{\circ}\text{C}/\text{decade}$  for the rest of the integration period, and a two-time scale response (initially fast, later slow) in the step-function doubling experiment.

Figures 3a and 3b compare the time evolution of zonally-averaged annual mean surface temperature changes in the Scenario A experiment for the signal Definitions 1 and 2. The space-time evolution of the signal differs for the two definitions, particularly at high latitudes in the Southern Hemisphere and in the first half of the integration. For Definition 1 (Figure 3a), high latitude temperature changes in both hemispheres are virtually monotonic. In contrast, the temperature response according to Definition 2 shows pronounced cooling at  $60^{\circ}\text{S}$ - $80^{\circ}\text{S}$  during the first half of the integration (Figure 3b). After 100 years, the response patterns for the two definitions are more similar, although the amplitude of the zonally-averaged response is larger for Definition 2. Both definitions show an interhemispheric asymmetry of the response, with a marked attenuation of the warming between ca.  $40^{\circ}\text{S}$ - $60^{\circ}\text{S}$ .

The zonally-averaged signal pattern in the  $2\times\text{CO}_2$  experiment according to Definition 1 (Figure 4a) is established within the first 10 years and remains relatively stable thereafter, gradually increasing in amplitude. The response poleward of  $60^{\circ}\text{S}$  is slower than the response poleward of  $60^{\circ}\text{N}$ , and the attenuation of warming between ca.  $40^{\circ}\text{S}$ - $60^{\circ}\text{S}$  is similar to the pattern seen in Scenario A.

The signal evolution in Scenario D (Definition 1) also shows marked interhemispheric differences (Figure 4b). Poleward of ca.  $70^{\circ}\text{N}$ , two distinct cooling episodes are separated by a warm period extending from years 20-40. Zonally-averaged temperature increases almost monotonically between  $60^{\circ}\text{S}$ - $80^{\circ}\text{S}$ , and there is little evidence of attenuated warming between  $40^{\circ}\text{S}$ - $60^{\circ}\text{S}$ .

The two-dimensional spatial patterns of annual mean surface air temperature change in the final decades of the three response experiments show a number of common features (Figures 2b-d):

- larger warming over land areas than over oceans;
- spatial co-location of large positive and negative anomalies between  $60^{\circ}\text{S}$ - $80^{\circ}\text{S}$ ;
- reduced warming relative to the zonal average (or even cooling) in the North Atlantic and North Pacific.

The major difference in the response patterns is the strong Arctic cooling in Scenario D, which is absent in the other experiments.

## 4 Statistical Analysis

The control run and the three greenhouse warming experiments were analysed statistically with respect to three separate properties: orthogonality, relative amplitudes, and time evolution of the signal and noise.

### 4.1 Orthogonality of Signal and Noise Patterns

Consider two sets of time-evolving spatial patterns,  $c(x, t)$  and  $s(x, t)$ , where  $x = 1, \dots, p$  and  $t = 1, \dots, n$  denote discrete space and time variables (model grid-points and years, respectively). We assume that we are dealing in the following with only one variable at one model level, and that  $c(x, t)$  and  $s(x, t)$  represent, respectively, data from the coupled model control integration and the Scenario A integration of Cubasch et al. (1992), e.g. 2m temperature, with  $p = 2048$  (for 2-d fields) or  $p = 480$  (for zonally-averaged data at 15 atmospheric levels) and  $n = 100$ . All results are for annually-averaged data, defined as anomalies relative to the smoothed initial state of the control integration (Definition 1), and are area-weighted, as in Cubasch et al. (1992).

The EOF representation of  $c(x, t)$  and  $s(x, t)$  is

$$c(x, t) = \sum_{j=1}^q \alpha_j^c(t) e_j^c(x) \quad (1)$$

$$s(x, t) = \sum_{j=1}^q \alpha_j^s(t) e_j^s(x) \quad (2)$$

$$x = 1, \dots, p; \quad t = 1, \dots, n$$

where  $e_j^c(x), e_j^s(x)$  are the EOFs of the control and response experiments, respectively,  $\alpha_j^c(t), \alpha_j^s(t)$  are the associated principal component (PC) time series, and the superscripts  $c$  and  $s$  are used to distinguish between control and signal data. The EOFs are defined without subtraction of the time means in order to preserve the full climate change signal and are normalized to form an orthonormal basis, i.e.,

$$\sum_{x=1}^p e_j^c(x) e_k^c(x) = \delta_{jk} \quad j, k = 1, \dots, q. \quad (3)$$

Note that the covariance matrices used for computing the EOFs are rank-deficient, so that the number of EOFs with non-zero eigenvalues is actually only  $q = \min(n - 1, p) = 99$  (see Preisendorfer, 1988).

The similarity of the dominant signal and noise patterns can be measured by the usual (centered) correlation

$$r = \sum_{x=1}^p (e_j^s(x) - \bar{e}_j^s)(e_j^c(x) - \bar{e}_j^c) / (p \sigma_j^s \sigma_j^c) \quad j = 1 \quad (4)$$

between the EOF 1 patterns of Scenario A and the control run, where  $\bar{e}_j^s, \bar{e}_j^c$  and  $\sigma_j^s, \sigma_j^c$  denote the spatial means and spatial standard deviations, respectively, of the Scenario A and control EOF 1 patterns. We also compute  $r^*$ , the uncentered form of (4), in which the spatial mean information is retained. Both definitions are useful. However, uncentered correlations are more appropriate in the present case, in which one is interested in comparing the total change which has occurred in two different experiments, including both the spatial mean and the superimposed variations about the spatial mean. The uncentered correlation is also consistent with the definition of the EOF patterns, in which the time mean was similarly retained. Theoretically, two patterns can yield correlation values  $r = 1, r^* = 0$  (if the spatial means are anticorrelated but the spatial anomalies are perfectly correlated and have the right amplitudes to cancel the mean term) or values  $r = 0, r^* = 1$  (if the patterns are dominated by a spatial mean term with small, uncorrelated spatial anomalies; see Richman and Lamb, 1985, and Santer et al., 1992).

Table 1 shows values of  $r$  and  $r^*$  for 10 different fields. A low value of  $r^*$  indicates that the dominant signal and noise patterns are dissimilar, a situation favorable for detection. The lowest values of  $r^*$  are for 2m temperature ( $r^* = 0.09$ ) and the vertical structure of the zonally-averaged u-velocity component ( $r^* = 0.36$ ), whereas SLP has the highest pattern correlation ( $r^* = 0.80$ ), indicating highly similar signal and noise patterns. The  $r$  and  $r^*$  values are generally comparable, except for 2m temperature ( $r = 0.43, r^* = 0.09$ ). In this case, the low value of the uncentered correlation reflects a large difference in the spatial means of the control and Scenario A EOF 1 patterns (despite normalization):  $\bar{e}_j^s$  is nearly six times larger than  $\bar{e}_j^c$ , since  $e_j^s(x)$  is positive at almost all grid-points (compare Figures 7a and 7b).

The control run EOF 1 pattern for the vertical profile of the u-velocity component has largest variance in the Southern Hemisphere, with a pronounced dipole structure extending throughout the model atmosphere (Figure 5a). This pattern is similar to that obtained by James and James (1989) in an experiment with a simple uncoupled atmospheric model. The dipole structure in the Southern Hemisphere is probably related to interannual variations in the latitudinal location of the subtropical jet. In contrast, the EOF 1 pattern for Scenario A (Figure 5b) has a strong signature in the lower strato-

sphere, where intensive cooling occurs and the intensity of the jet cores increases in both hemispheres and in both seasons.

A pronounced vertical temperature contrast (stratospheric cooling and tropospheric warming) is a common feature of the greenhouse-gas signals simulated in a number of different model experiments (e.g. Schlesinger and Mitchell, 1987; Cubasch et al., 1992). Recently, Karoly (1987, 1989) has compared such signals with observations, and suggests that vertical temperature contrasts could be useful for detecting greenhouse-gas-induced climatic change. However, as Liu and Schuurmanns (1990) and Wigley and Barnett (1990) have pointed out, this characteristic signal may resemble the observed pattern of vertical temperature changes associated with low-frequency internally-generated natural variability. Our results suggest that the overall structure of the dominant control run EOF for vertical temperature changes is correlated with the EOF 1 pattern of Scenario A ( $r^* = 0.57$ ; see Table 1), mainly due to the correspondence of signal and noise patterns in the tropical troposphere and stratosphere (see Figures 5c,d). In the case of the noise EOF this is probably due to changes in convective activity and the height of the tropopause associated with the overall cooling trend in the control run.

The dominant noise and signal EOFs of vertically-integrated precipitable water (Figures 6a,b) are also correlated ( $r^* = 0.65$ ). The signal EOF is spatially coherent, and is characterized by hemispheric and zonal symmetry, with highest variance in the tropics and low variance towards the poles. This describes mainly the change in mean state (increases in precipitable water at virtually all grid-points, with the largest increases over the tropical oceans). The first EOF of the control run, although less coherent spatially, also tends to have largest variance in the tropics. We include the case of SLP ( $r^* = 0.80$ ; see Figures 6c,d) in order to show an unfavorable case for signal detection, where the first noise and signal EOFs are both characterized by strong zonal structure in the vicinity of the Antarctic Circumpolar Trough.

The spatial patterns of the dominant surface temperature EOFs show a number of interesting features (Figures 7a-d). First, the EOF 1 patterns of three greenhouse warming experiments (IPCC Scenarios A and D, and a  $2\times\text{CO}_2$  experiment) are very similar, despite the differences in forcing history (see Table 2). This similarity is primarily due to a common land-sea contrast component.

Second, the EOF 1 patterns in the Scenario A and  $2\times\text{CO}_2$  experiments are only weakly correlated with the dominant noise mode ( $r^* = 0.09$  and  $r^* = 0.05$ , respectively; see Table 2). We note, however, that the variability exhibited in the region of the Antarctic Circumpolar Current (ACC) is at least qualitatively similar in the first EOFs of the control run and the three greenhouse warming integrations (see Figure 7). In the control run – unlike Scenario A and  $2\times\text{CO}_2$  – the variability in the Ross and Weddell Seas is generally out of phase with variability in the tropics and in the Northern Hemisphere (Figure 7a).

The correlation between the EOF 1 patterns of the control and Scenario D is higher ( $r^* = 0.66$ ), partly because changes in the Arctic and in the ACC are also in phase.

Third, the high pattern correlation between EOF 2 of Scenario A (which explains only 3.1% of the variance) and EOF 1 of the control run ( $r^* = 0.75$ ; see Table 2 and Figures 7a, 8b) suggests at least a small common component of natural variability and/or drift in the two experiments. There is no evidence for such a common component in the 2xCO<sub>2</sub> experiment ( $r^* = 0.39$  for EOF 1 control versus EOF 2 of 2xCO<sub>2</sub>).

## 4.2 Signal-to-Noise Ratios

Centered pattern correlations yield only a measure of the similarity of the normalized signal and noise patterns, but provide no information on the relative amplitudes of different EOFs. Various measures can be defined to provide such information.

We compare first the number of EOFs required to explain 95% of the variance of the control run ( $k_c$ ) and Scenario A data ( $k_s$ ; see Table 3).  $k_c$  and  $k_s$  are measures of the spatio-temporal coherence and amplitude of signal and noise.  $k_c$  is largest for variables with limited spatial coherence, such as precipitation rate ( $k_c = 80$ ) and total cloud cover ( $k_c = 84$ ), and smallest for variables with highly coherent spatial structures, e.g. vertical temperature contrasts ( $k_c = 24$ ). In the Scenario A data,  $k_s$  is smallest for variables characterized by spatially-coherent signals of large amplitude, e.g. vertical temperature contrast ( $k_s = 1$ ) and 2m temperature ( $k_s = 19$ ). The results indicate that vertical temperature contrast, the vertical structure of zonal winds, 2m temperature and precipitable water are associated with low-dimensional response signals embedded in a much higher-dimensional noise space.

Next we consider how much of the variance of the Scenario A data lies in the truncated space of the first 99 control run EOFs, or, alternatively, how much of the control run variance lies in the first 99 EOFs of Scenario A. For this purpose we form the projections (identified by two superscripts, the first denoting the data set represented in the projection and the second the data set used for computing the EOFs)

$$\alpha_j^{sc}(t) = \sum_{x=1}^p s(x, t) e_j^c(x) \quad (5)$$

and

$$\alpha_j^{cs}(t) = \sum_{x=1}^p c(x, t) e_j^s(x) \quad (6)$$

$$j = 1, \dots, q; \quad t = 1, \dots, n$$

and compute the ratios of the variance of the projection relative to the variance of the original data set

$$V_q^{sc} = \frac{\sum_{j=1}^q \sum_{t=1}^n \alpha_j^{sc}(t)^2}{\sum_{x=1}^p \sum_{t=1}^n s(x, t)^2} \quad (7)$$

$$V_q^{cs} = \frac{\sum_{j=1}^q \sum_{t=1}^n \alpha_j^{cs}(t)^2}{\sum_{x=1}^p \sum_{t=1}^n c(x, t)^2} \quad (8)$$

$V_q^{sc}$  and  $V_q^{cs}$  are measures of the overall orthogonality of signal and noise data sets. The results are a little surprising. For total cloud cover, for example, only 32.4% (32.8%) of the total Scenario A (control) variance can be explained by the projection onto the first 99 control (Scenario A) EOFs, while for the zonally-averaged u-velocity component, virtually all of the variance of the original data sets can be explained by the projection onto either signal or noise EOFs. Does this imply that the ‘detection potential’ of changes in cloud cover is high? Probably not. We know from the  $k_c$  and  $k_s$  results (Table 3) and from visual inspection of the EOF patterns that cloud cover is extremely noisy spatially in both Scenario A and control data sets. A time-history PC selection rule (Rule Q; Preisendorfer, 1988) also revealed that the control and signal PC time series for cloud cover (for PCs higher than 2) were indistinguishable from temporal white noise. For variables such as total cloud cover and precipitation rate, where both  $k_c$  and  $k_s$  are large,  $V_q^{sc}$  and  $V_q^{cs}$  are not meaningful indicators of the true orthogonality of signal and noise. This is due to the problem of estimating the EOFs of a high-dimensional signal and noise when the spatial dimension  $p$  is many times larger than the number of time samples  $n$ .  $V_q^{sc}$  and  $V_q^{cs}$  are useful indicators of orthogonality only when the signal and noise can be characterized by a relatively small number of EOFs (i.e., when  $k_c$  and  $k_s$  are much smaller than  $n$ ), and the EOFs can be estimated reliably.

The  $V_q^{sc}$  and  $V_q^{cs}$  results are not very sensitive to whether the signal is projected onto the noise EOFs or the noise is projected onto the signal EOFs. Exceptions are 2m temperature and precipitable water. In the former case, the explained variance is much lower for the projection of the signal onto the noise EOFs (66.4% for  $V_q^{sc}$  vs. 81.8% for  $V_q^{cs}$ ). This difference is due to the fact that the dominant EOF 1 pattern of Scenario A (see Figure 7b), which is spatially coherent and represents warming at almost all grid-points, is not represented in the control run. In the case of precipitable water,  $V_q^{cs}$  is smaller than  $V_q^{sc}$  largely because the EOF 1 pattern of the control run is more strongly represented in the signal than the EOF 1 pattern of the signal is represented in the noise (see Figures 6a,b).

These results are confirmed by  $V_1^{sc}$ ,  $V_1^{cs}$ ,  $V_2^{sc}$ , and  $V_2^{cs}$ , which are defined analogously

to  $V_q^{sc}$  and  $V_q^{cs}$ , but with the projections restricted to EOF 1 and EOF 2 of signal and noise. e.g.,

$$V_1^{sc} = \sum_{t=1}^n \alpha_1^{sc}(t)^2 / \sum_{x=1}^p \sum_{t=1}^n s(x, t)^2 \quad (9)$$

$$V_2^{sc} = \sum_{t=1}^n \alpha_2^{sc}(t)^2 / \sum_{x=1}^p \sum_{t=1}^n s(x, t)^2 \quad (10)$$

$V_1^{sc}$  and  $V_2^{sc}$  provide insight into the extent to which the signal is contaminated by the individual dominant noise modes. For precipitable water, SLP and the vertical signal in temperature and meridional winds, the signal is strongly contaminated by the EOF 1 mode of the control run. This situation is unfavorable for detection. Contamination of the signal by the first noise mode is lowest for 2m temperature ( $V_1^{sc} = 2.6\%$ ). The fact that  $V_2^{cs}$  is large (30.2%) for 2m temperature when the noise is projected onto Scenario A EOF 2, but small when the signal is projected onto the control EOF 2 ( $V_2^{sc} = 2.1\%$ ) indicates that there is a common natural variability or drift component, but its amplitude is much larger in the control run than in Scenario A.

### 4.3 Time Evolution of Signal and Noise

Having discussed the spatial structures of the signal and noise patterns, we turn now to the evolution of the patterns with time. This is necessary to determine whether and at what point in time we could expect to detect a model-predicted greenhouse-gas signal. The time evolution is analysed in three different ways: using cumulative EOF contributions to the explained spatial variance, PC time series, and projections of signal and noise data onto pairs of either signal or noise EOFs. We use these techniques here only as descriptive tools, to compare the behavior of climate variables with different signal and noise time evolution properties. Quantitative estimates of detection times are derived in Part 2 of this study (Santer et al., 1993).

#### 4.3.1 Cumulative Explained Variance

A useful description of the time evolution of the contribution of different EOFs to the variance of the signal is given by the cumulative explained variance, defined by

$$V_{q'}^{ss}(t) = \sum_{j=1}^{q'} \alpha_j^{ss}(t)^2 / \sum_{x=1}^p s(x, t)^2 \quad (11)$$

with  $t = 1, \dots, n$ ;  $1 \leq q' \leq q$

where  $\alpha_j^{ss}(t)$  is the projection of the Scenario A anomaly data onto the EOFs of Scenario A. For  $q' = q$ , the spatial variance of the original anomaly data is completely recaptured and  $V_q^{ss}(t)$  is unity at each time  $t$ .

Figure 9a shows the cumulative explained spatial variance as a function of time and number of EOFs ( $q' = 1, 2, 10, 20$  and  $50$ ) for annually-averaged temperature in Scenario A (Definition 1). As noted in Cubasch et al. (1992), the temperature signal in the first 20-30 years of the experiment is comprised of a large number of patterns, while in the second half of the experiment a single dominant pattern emerges. The variance explained by the first EOF increases almost monotonically over the first 65 years, reaching an asymptotic value of 90-95%. The corresponding results for Definition 2 (Figure 9b) indicate that the emergence of a single dominant signal pattern in the second half of the Scenario A experiment is independent of the way in which the signal is defined. This is, in fact, a property of any non-stationary signal which grows with time, for which the variance is dominated by the later stages of the signal.

A different picture is obtained for the  $2xCO_2$ , Scenario D and control integrations (Figures 10a-c). In the  $2xCO_2$  integration, in which the initial response is much more rapid, a single dominant signal pattern is established within the first 15-20 years (at which point EOF 1 explains over 80% of the spatial variance), the contribution from EOF 2 being much smaller than in the case of Scenario A during the entire period. At the end of the Scenario D experiment, a single dominant pattern has not yet emerged. The first EOF explains less than 70% of the variance, and more than 20 patterns are required in order to explain over 90% of the spatial variance. Note also that the contribution from EOF 2, which is very similar to the EOF 2 mode of the control run (see Table 2 and Figures 8a, 8c), is in fact larger than that of EOF 1 during decades 3 and 4, decreasing to a few percent between years 50-80, but increasing again towards the end of the experiment. This indicates some contamination of the surface temperature signal in Scenario D by the natural variability and/or drift of the control run, as found also for the EOF 2 mode of Scenario A (which was highly correlated with EOF 1 of the control run; see Table 2). In the case of the control run, the dominant mode of variability evolves in a complex way, with several fluctuations on decadal timescales. The maximum spatial variance explained by the first EOF is approximately 80% after 60 years.

In the case of SLP, the cumulative explained spatial variance results are extremely noisy (Figure 11a), and for Scenario A there is no clear evidence of an evolving signal in the first few EOF modes. In contrast, for total precipitation rate there is a gradually evolving signal in Scenario A, which explains roughly 30% of the total spatial variance after 100 years (Figure 11b). Since precipitation rate is spatially very noisy, the number of patterns required to explain a given level of the spatial variance is higher than in the

case of SLP or 2m temperature.

### 4.3.2 Principal Component Time Series

Another way of comparing the temporal behavior of signals and noise on a common basis is to project data from the greenhouse warming experiments and the control run onto a common set of EOFs. We first projected anomaly data from all four integrations onto the Scenario A EOFs. As noted in Cubasch et al. (1992), the projection of the control run data onto EOF 1 of Scenario A is close to zero, thus confirming the orthogonality of the dominant signal and noise modes (see Figure 12a). In contrast, the control run has a large projection on EOF 2 of Scenario A (Figure 12b), a result which supports our earlier conclusion (Section 4.2 and Table 3) that this component of the signal in Scenario A, although not very large, is similar to the variability seen in the control run. Note that this component is very much smaller in the 2xCO<sub>2</sub> experiment.

We used also the control run EOFs as our set of common basis pattern set (Figure 13). For the control run, PC 1 can be closely identified with the large-scale cooling, showing the same decadal timescale fluctuations which were evident in Figure 10c. The amplitude of this mode is much larger in the control run than in the other three experiments. In the greenhouse warming experiments, the amplitude of this component is largest in Scenario D, increasing monotonically with time. As noted previously, this result is largely due to the similarity of the variability in the Arctic and the ACC in these two experiments. The PC time series of Scenarios A and D evolve similarly until year 50, after which time the Scenario A PC decreases in magnitude, while the magnitude of the Scenario D PC continues to increase slowly.

These results confirm the analysis of the pattern correlations and the signal-to-noise ratios. The amplitude of the common variability and/or drift component is largest at the end of the Scenario D experiment. It is also large between years 30-50 of the Scenario A experiment, and is generally small in the 2xCO<sub>2</sub> experiment.

We also used the pattern projection technique to determine the contribution of the land-sea contrast (which can be expected to imprint its signature on the climate response because of the larger heat storage in the ocean) to the greenhouse warming signal. For this purpose we projected the anomaly data from the four experiments onto the model's land-sea mask, defined as:

$$m(x) = \begin{cases} N & \text{if } x \text{ is a land grid-point} \\ 0 & \text{if } x \text{ is an ocean grid-point} \end{cases}$$

where the normalizing constant  $N$  was chosen such that

$$\sum_{x=1}^p m(x)^2 = 1$$

For the Scenario A data the projection coefficients are thus defined as

$$\gamma^{sm}(t) = \sum_{x=1}^p s(x,t) m(x) \quad t = 1, \dots, n \quad (12)$$

The resultant principal component time series, shown in Figure 14, are very similar to the PC time series for the projection of the data onto EOF 1 of Scenario A (see Figure 12a). Thus a simple pattern of zeroes over ocean points and ones over land points, with no zonal or meridional information (other than the number of land versus ocean grid-points as functions of latitude and longitude) reproduces much of the information contained in the Scenario A EOF 1 pattern. The fraction of the total space-time variance explained by the land-sea mask pattern, given by

$$V_1^{sm} = \sum_{t=1}^n \gamma^{sm}(t)^2 / \sum_{x=1}^p \sum_{t=1}^n s(x,t)^2 \quad (13)$$

is 27.6% and 27.9% for Scenario A and the 2xCO<sub>2</sub> experiment (respectively). For Scenario D and the control run the corresponding figures are 3.6% and 2.8%. Thus land-sea contrast is a significant component of the signal in the Scenario A and CO<sub>2</sub>-doubling experiments, but is less important in Scenario D and in the control run. Note, however, that these figures are still considerably smaller than the variance explained by the 2m temperature EOF 1 patterns (see Table 2).

### 4.3.3 Projections in Two-Dimensional EOF-Space

One further way of examining the joint evolution of signal and noise in both time and space is by considering the projections of signal and noise data on pairs of either control or signal EOFs (see Preisendorfer, 1988). Consider, for example, the projection of the control run and Scenario A 2m temperature data onto the first two EOFs of Scenario A (Figure 15a). Each symbol on the figure represents one year of the control run or Scenario A. If there were no temporal coherence in the evolution of signal and noise, both would be represented in EOF-space by random distributions of points. Clearly, this is not the case. At year 1, the two integrations occupy approximately the same location in EOF-space. Thereafter signal and noise rapidly evolve along divergent paths, the signal towards increasing warming and the control run towards increasing cooling. As noted

previously, the common variability and/or drift component is limited to EOF 2 – the control run has virtually no projection on EOF 1 and a large projection on EOF 2.

This result suggests that, in the case of 2m temperature, it should be easier to discriminate signal from noise in EOF 1-space rather than in the combined space of the first two EOFs. When we remove the major source of information about the signal (EOF 1) and instead project on EOFs 2 and 3 of Scenario A, there is clearly a much greater degree of overlap between the signal and noise clouds (Figure 15b).

Essentially the same qualitative picture results if the projection basis is changed from the Scenario A EOFs (Figure 15a) to the control run EOFs (Figure 16). The main difference is that the control run and Scenario A now require slightly longer (over two decades) to separate.

Figure 17 shows the analogous projection of the control run and the Scenario D 2m temperature data on the first two Scenario D EOFs. For the first three to four decades, both integrations follow very similar trajectories. Scenario D begins to emerge from the noise cloud only within the last few decades of the experiment. Note that the control run has large projections on both EOFs of Scenario D.

Finally, we considered a case where signal and noise are less easily separable, and projected the control run and Scenario A SLP data onto the first two EOFs of the Scenario A SLP data (Figure 18). The time evolution of signal and noise is more random than in the case of temperature, and there is considerable overlap between the clouds of points in EOF-space.

The noise cloud in these figures can be thought of as an envelope encompassing all locations in EOF-space which the coupled ocean-atmosphere model ‘visits’ in the course of natural fluctuations of the coupled system. Clearly, we need to have information about all possible natural variability trajectories in order to adequately describe the statistical properties of the noise cloud. The problem of detecting a greenhouse-gas signal depends crucially on how well these properties can be estimated. A single control integration performed with a single model is obviously inadequate. Results from different models, or from multiple integrations in which a single model is run with the same forcing but starting from different initial conditions (Cubasch et. al., 1993), will clearly be required in order to establish the statistical properties of both signal and noise clouds, and to decide whether a given signal trajectory falls outside the statistical confidence limits of the natural variability trajectories.

## 5 Summary and Conclusions

For detection studies, we would like to focus on variables whose signal and noise patterns are highly dissimilar (Barnett and Schlesinger, 1987). The more similar the signal and noise patterns, the more difficult it is to distinguish between natural variability and the greenhouse-gas signal. We used the spatial correlation between the EOF 1 patterns of the control run and the Scenario A experiment as a measure of the similarity of signal and noise patterns. Our results suggest that 2m temperature and vertical changes in zonally-averaged winds (u-component) have dissimilar signal and noise patterns (with typically less than 25% common variance between the signal and noise EOF 1 patterns), a situation favorable for detection. The dominant signal and noise patterns are more similar for vertical temperature contrasts and vertically-integrated precipitable water. Some features require further investigation, in particular the similarity of signal and noise patterns for vertical temperature contrasts in the tropical troposphere and stratosphere, and the similarity between signal and noise 2m temperature patterns in the vicinity of the Antarctic Circumpolar Current. Sea level pressure has highly similar signal and noise EOF 1 patterns, and is unlikely to be a useful component of a multivariate “fingerprint” detection vector.

The spatial EOF analysis indicated that 2m temperature, precipitable water, and the vertical distribution of zonal temperature and zonal winds are characterized by low-dimensional signals embedded in a higher-dimensional noise space. In contrast, cloud cover and precipitation rate have high-dimensional signals and noise.

To determine the degree to which the signal was contaminated by the natural variability (and/or drift) of the control, we projected the Scenario A data onto EOFs 1 and 2 of the control. Signal contamination by the control run EOF 1 and 2 modes was lowest for 2m temperature. The signals for precipitable water, SLP, and the vertical structure of zonal temperature and zonal winds were significantly contaminated by the dominant noise modes. A further interesting result was that land-sea contrast constitutes a significant component of the 2m temperature signal in the Scenario A and 2xCO<sub>2</sub> integrations, explaining over 25% of the total space-time variance of the anomaly data in both experiments.

We used cumulative explained spatial variance, principal component time series, and projections onto EOF pairs in order to investigate the time evolution of the dominant signal and noise modes. For 2m temperature, a single pattern emerges as the dominant signal component in the second half of the Scenario A experiment. This result is not sensitive to the precise definition of the signal. The time evolution of the dominant patterns is different in the 2xCO<sub>2</sub>, Scenario D, and control integrations. The principal component time series and projections onto EOFs 1 and 2 of the control run indicate that

the control run and Scenario D have a large common variability and/or drift component. This common component is also large between years 30-50 of the Scenario A experiment, but is small in the 2xCO<sub>2</sub> integration. For 2m temperature, the trajectories of Scenario A and the control run modes evolve divergently in the EOF 1 – EOF 2 plane, regardless of the basis vectors chosen for projection, thus making it feasible to separate signal and noise within the first two decades of the experiments. For Scenario D, the trajectory in the EOF plane suggests that it would not be possible to discriminate between the dominant signal and noise modes until the final 2-3 decades of the 100-year integration.

It should be pointed out that the signal-to-noise results presented here are subject to various uncertainties, arising in particular from errors due to the so-called “cold start” problem (Hasselmann et al., 1992) and from the difficulties of discriminating between drift and natural variability.

The cold start problem is related to the experimental design (Cubasch et al., 1992; Hasselmann et al., 1992). All time-dependent experiments with the coupled ocean-atmosphere model considered here were initialized with both atmosphere and ocean at equilibrium with respect to an equivalent CO<sub>2</sub> concentration of 360 ppmv, approximately corresponding to 1985 concentrations. Using linear response theory, Hasselmann et al. (1992) estimated that the neglect of greenhouse-gas forcing history prior to 1985 may lead to an error of roughly 0.4°C after 50 years in the Scenario A integration. A rigorous resolution of the cold start problem would require greenhouse warming experiments commencing in 1900 or earlier.

From the single control run carried out here it is also difficult to separate clearly the contributions to the non-stationarity of the control run from a possible residual drift (associated with failure of the flux correction technique to balance exactly the fluxes of heat, momentum and freshwater between atmosphere and ocean) or from the internal natural variability. The control run changes probably involve both factors. The signal-to-noise results presented here may need to be modified if drift is found to be responsible for most of the long-term control run variations. However, we anticipate that, since the largest flux corrections tend to be in areas where the natural variability of the climate system is also large (e.g., at sea-ice margins), the signal-to-noise orthogonality properties may not be very sensitive to uncertainties regarding drift. In order to clarify the issue of drift versus natural variability, longer control integrations ( $\geq 200 - 300$  years) with the coupled model are needed. Further improvements in model physics are also required to reduce the magnitude of the flux corrections and the residual flux correction imbalances.

Not addressed here is the question of the statistical significance of the computed response and the estimation of detection times. This is discussed in Part 2 of this paper (Santer et al., 1993). The present results suggest that the near-surface temperature field might be a suitable candidate for the detection of a greenhouse-gas signal. However, we

have not addressed the problem of distinguishing between a greenhouse-gas signal and the response to other possible external forcing, such as solar variability or sulfate aerosols. Recent experiments by Oglesby (1992), for example, show similar patterns in response to greenhouse-gas forcing and solar constant changes for surface temperature, but different patterns for the vertical temperature structure. In order to discriminate between different external forcing mechanisms and between external forcing and internal natural variability, general optimal detection “fingerprint” techniques are required which consider the full four-dimensional space-time structure of the signals and noise (e.g. Hasselmann, 1993).

## Acknowledgements

This work was sponsored by the Bundesministerium für Forschung und Technologie, the Commission of the European Community, the Max-Planck-Gesellschaft and the Freie and Hansestadt Hamburg. The authors would like to thank the staff of the Deutsches Klimarechenzentrum, the Meteorologisches Institut der Universität Hamburg and the Max-Planck-Institut für Meteorologie for their support, in particular Hans von Storch, Mojib Latif and Gabi Hegerl. We also thank Tim Barnett, Larry Gates, Karl Taylor and Tom Wigley for valuable comments and suggestions.

## References

- Barnett TP (1986) Detection of changes in the global tropospheric temperature field induced by greenhouse gases. *J Geophys Res* 91:6659-6667
- Barnett TP, Schlesinger ME (1987) Detecting changes in global climate induced by greenhouse gases. *J Geophys Res* 92:14772-14780
- Barnett TP (1991) An attempt to detect the greenhouse-gas signal in a transient GCM simulation. In: Schlesinger ME (ed) *Greenhouse-Gas-Induced Climatic Change: A Critical Appraisal of Simulations and Observations*. Elsevier, Amsterdam, pp 559-568
- Cess RD, Potter GL, Blanchet JP, Boer GJ, Ghan SJ, Kiehl JT, Le Treut H, Li ZX, Liang XZ, Mitchell JFB, Morcrette J-J, Randall DA, Riches MR, Roeckner E, Schlese U, Slingo A, Taylor KE, Washington WM, Wetherald RT, Yagai I (1989) Interpretation of cloud climate feedback as produced by 14 atmospheric general circulation models. *Science* 245:513-516
- Cubasch U, Hasselmann K, Höck H, Maier-Reimer E, Mikolajewicz U, Santer BD, Sausen R (1992) Time-dependent greenhouse warming computations with a coupled ocean-atmo-

sphere model. *Climate Dynamics* (In press)

Cubasch U, Santer BD, Hellbach A, Hegerl G, Höck H, Maier-Reimer E, Mikolajewicz U, Stössel A, Voss R (1993) Monte Carlo climate change forecasts with a global coupled ocean-atmosphere model (Submitted to *Climate Dynamics*)

Hasselmann K (1993) Optimal fingerprints for the detection of time dependent climate change (Submitted to *J Climate*)

Hasselmann K, Sausen R, Maier-Reimer E, Voss R (1992) On the cold start problem in transient simulations with coupled ocean-atmosphere models. (Submitted to *Climate Dynamics*)

Houghton JT, Jenkins GJ, Ephraums JJ (1990) *Climate Change. The IPCC Scientific Assessment*. Cambridge University Press, Cambridge, 365 pp

James IN, James PM (1989) Ultra-low-frequency variability in a simple atmospheric circulation model. *Nature* 342:53-55

Karoly DJ (1987) Southern Hemisphere temperature trends: A possible greenhouse gas effect? *Geophys Res Lett* 14:1139-1141

Karoly DJ (1989) Northern Hemisphere temperature trends: A possible greenhouse gas effect? *Geophys Res Lett* 16:465-468

Lautenschlager M, Herterich K (1990) Atmospheric response to ice age conditions – climatology near the earth's surface. *J Geophys Res* 95:22547-22557

Liu Q, Schuurmanns CJE (1990) The correlation of tropospheric and stratospheric temperatures and its effect on the detection of climate changes. *Geophys Res Lett* 17:1085-1088

MacCracken MC, Moses H (1982) The first detection of carbon dioxide effects: Workshop Summary, 8-10 June 1981, Harpers Ferry, West Virginia. *Bull Amer Met Soc* 63:1164-1178

Madden RA, Ramanathan V (1980) Detecting climate change due to increasing carbon dioxide. *Science* 209:763-768

Maier-Reimer E, Hasselmann K (1987) Transport and storage of CO<sub>2</sub> in the ocean – an inorganic ocean-circulation carbon cycle model. *Climate Dynamics* 2:63-90

Maier-Reimer E, Mikolajewicz U (1989) Experiments with an OGCM on the cause of the Younger Dryas. In: Ayala-Castanares A, Wooster W, Yanez-Arancibia A (eds) *Oceanography 1988*. UNAM Press. Mexico, pp 87-100

Maier-Reimer E, Mikolajewicz U, Hasselmann K (1993) On the sensitivity of the global ocean circulation to changes in the surface heat flux forcing. *J Phys Oceanogr* (In press)

Manabe S, Stouffer RJ, Spelman MJ, Bryan K (1991) Transient responses of a coupled ocean-atmosphere model to gradual changes of atmospheric CO<sub>2</sub>. Part I: Annual mean response. *J Climate* 4:785-818

Mikolajewicz U, Maier-Reimer, E (1990) Internal secular variability in an ocean general circulation model. *Climate Dynamics* 4:145-156

Mikolajewicz U, Santer BD, Maier-Reimer E (1990) Ocean response to greenhouse warming. *Nature* 345:589-593

Mikolajewicz U, Maier-Reimer E, Barnett TP (1992) Acoustic detection of greenhouse-induced climate changes in the presence of slow fluctuations of the thermohaline circulation. *J Phys Oceanogr* (In press)

Oglesby RJ (1992) Personal communication

Preisendorfer RW (1988) Principal component analysis in meteorology and oceanography. *Developments in Atmospheric Science* 17, Elsevier, Amsterdam, 425 pp

Richman MB, Lamb PJ (1985) Climatic pattern analysis of three- and seven-day summer rainfall in the central United States: Some methodological considerations and a regionalization. *J Clim Appl Met* 24:1325-1343

Roeckner E, Dümenil L, Kirk E, Lunkeit F, Ponater M, Rockel B, Sausen R, Schlese U (1989) The Hamburg version of the ECMWF model (ECHAM). In: Boer GF (ed) *Research Activities in Atmospheric and Oceanic Modelling*. CAS/JSC Working Group on Numerical Experimentation 13:7.1-7.4 WMO Technical Document 322, Geneva

Santer BD, Wigley TML, Schlesinger ME, Jones PD (1991) Multivariate methods for the detection of greenhouse-gas-induced climate change. In: Schlesinger ME (ed) *Greenhouse-Gas-Induced Climatic Change: A Critical Appraisal of Simulations and Observations*. Elsevier, Amsterdam, pp 511-536

Santer BD, Wigley TML, Jones PD (1992) Correlation methods in fingerprint detection studies. *Climate Dynamics* (In press)

Santer BD, Brüggemann W, Cubasch U, Hasselmann K, Höck H, Maier-Reimer E, Mikolajewicz U (1993) Signal-to-noise analysis of time-dependent greenhouse warming experiments. Part 2: Estimates of Detection Time (In preparation)

Sausen R, Barthel K, Hasselmann K (1988) Coupled ocean-atmosphere models with flux corrections. *Climate Dynamics* 2:154-163

Schlesinger ME, Mitchell JFB (1987) Climate model simulations of the equilibrium climatic response to increased carbon dioxide. *Rev of Geophys* 25:760-798

Stouffer RJ, Manabe S, Bryan K (1989) Interhemispheric asymmetry in climate response to a gradual increase of atmospheric CO<sub>2</sub>. *Nature* 342:660-662

Washington WM, Meehl GA (1989) Climate sensitivity due to increased CO<sub>2</sub>: Experiments with a coupled atmosphere and ocean general circulation model. *Climate Dynamics* 4:1-38

Wigley TML, Barnett TP (1990) Detection of the greenhouse effect in the observations. In: Houghton JT, Jenkins GJ, Ephraums JJ (eds) *Climate Change. The IPCC Scientific Assessment*. Cambridge University Press, Cambridge, pp 239-256

Wigley TML, Jones PD (1981) Detecting CO<sub>2</sub>-induced climatic change. *Nature* 292:205-208



**Figure 9a.** Cumulative explained spatial variance of annually-averaged 2m temperature change (Definition 1) for Scenario A as a function of time and number of EOFs (1, 2, 10, 20, 50).

**SCENARIO A: 2M TEMPERATURE (DEFINITION 1)**

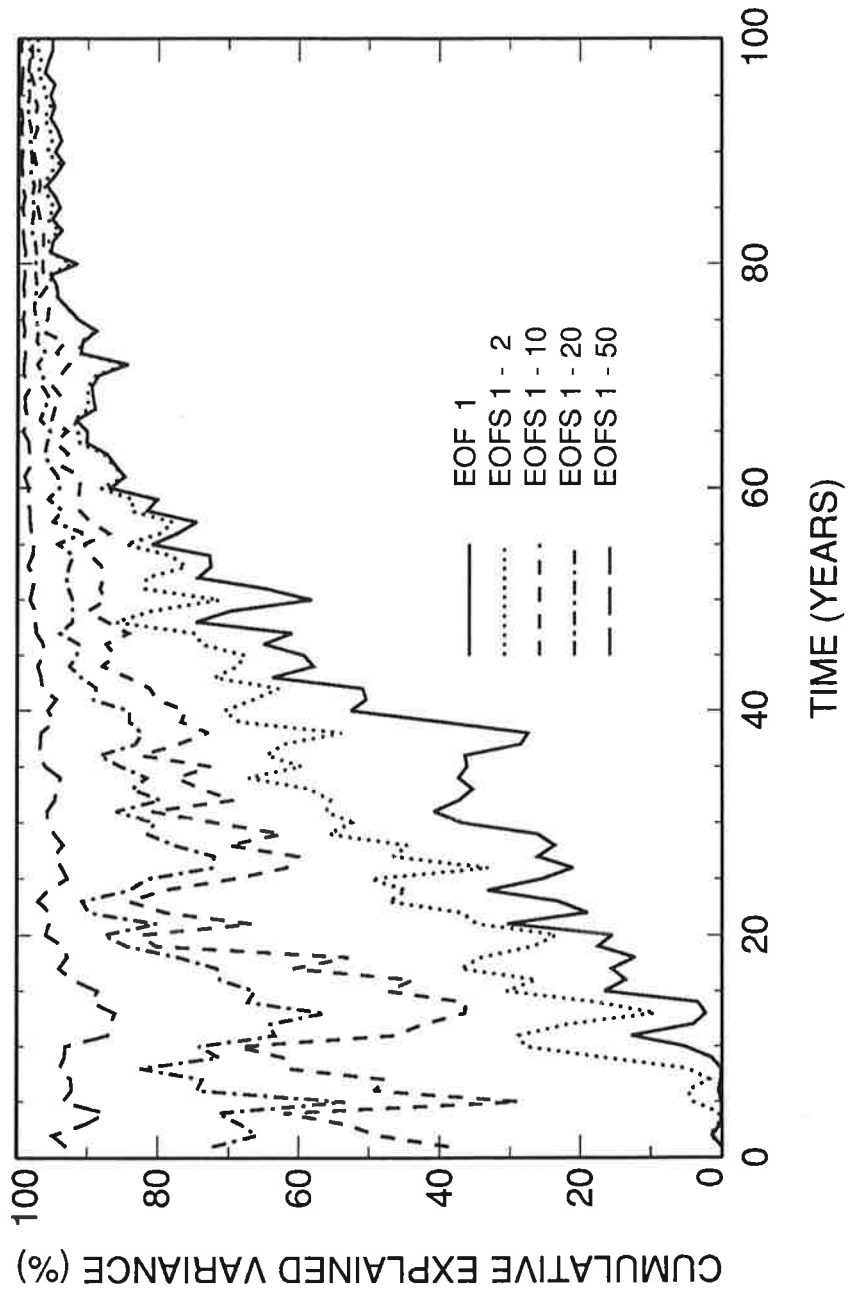


**Figure 9b.** Cumulative explained spatial variance of annually-averaged 2m temperature change (Definition 2) for Scenario A as a function of time and number of EOFs (1, 2, 10, 20, 50). The emergence of a single dominant signal pattern in the second half of the Scenario A experiment is independent of the way in which the signal is defined (see figure 9a).

### SCENARIO A: 2M TEMPERATURE (DEFINITION 2)

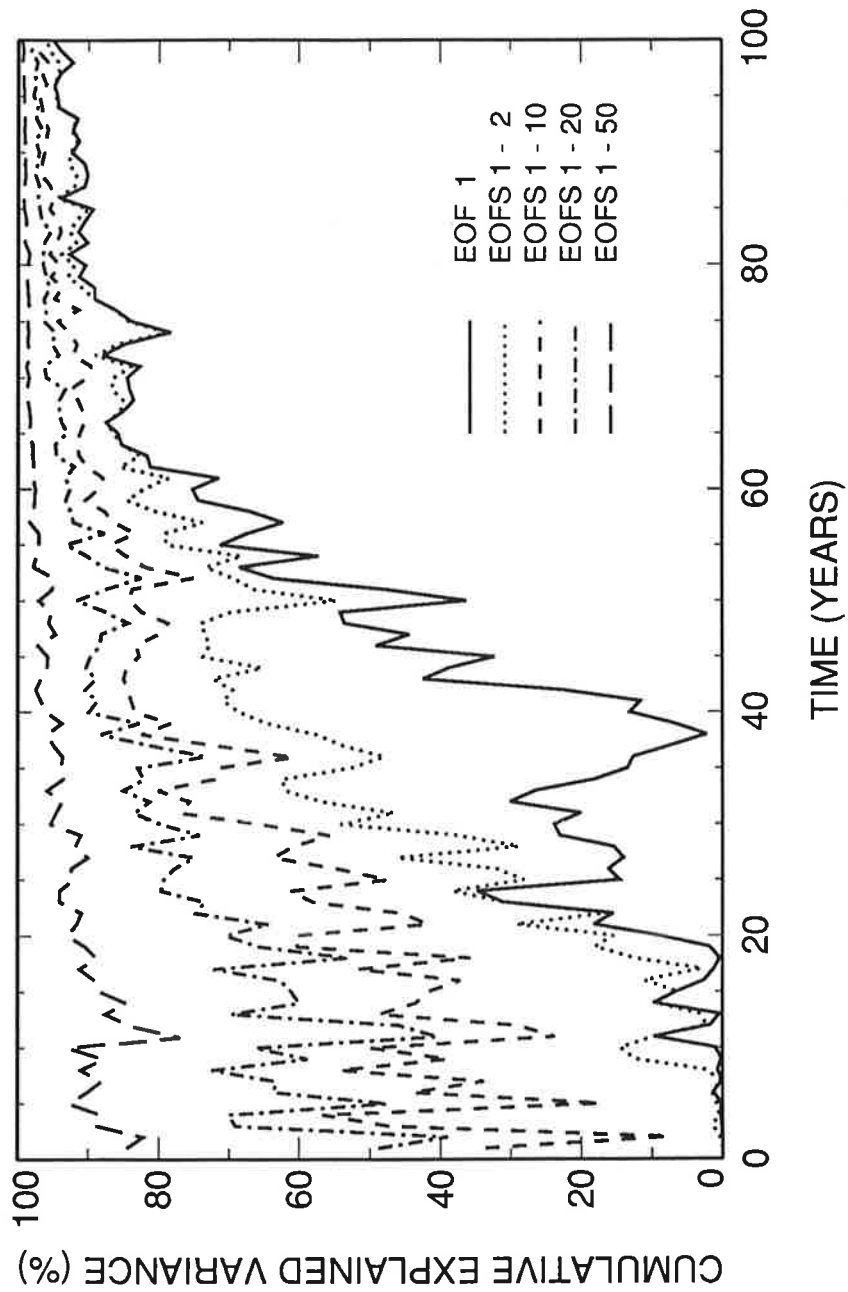


**Figure 10a.** Cumulative explained spatial variance of annually-averaged 2m temperature change (Definition 1) as a function of time and number of EOFs (1, 2, 10, 20, 50) in the 2xCO<sub>2</sub> experiment.

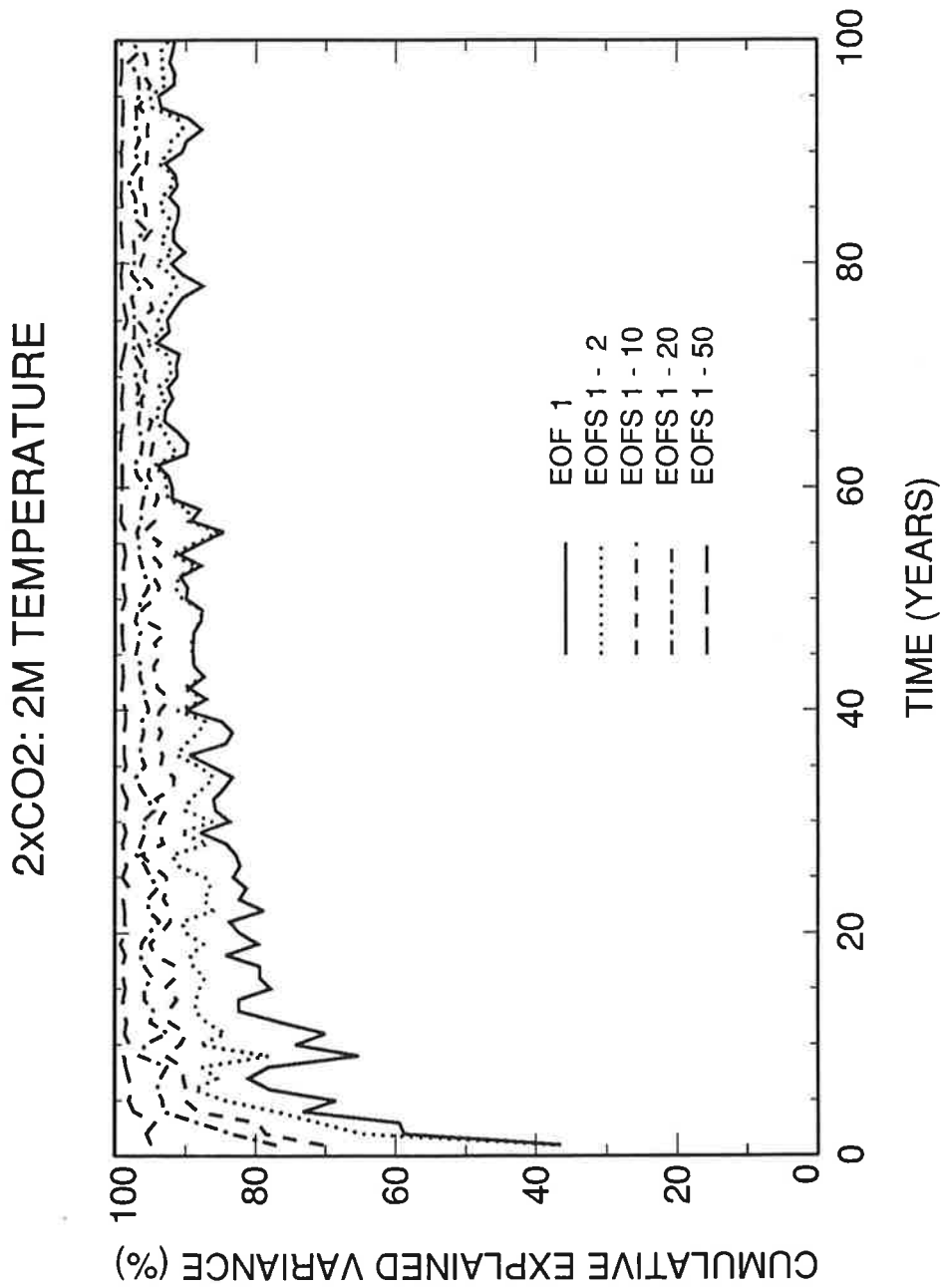


Figure 10b. Cumulative explained spatial variance of annually-averaged 2m temperature change (Definition 1) as a function of time and number of EOFs (1, 2, 10, 20, 50) for Scenario D.

### SCENARIO D: 2M TEMPERATURE

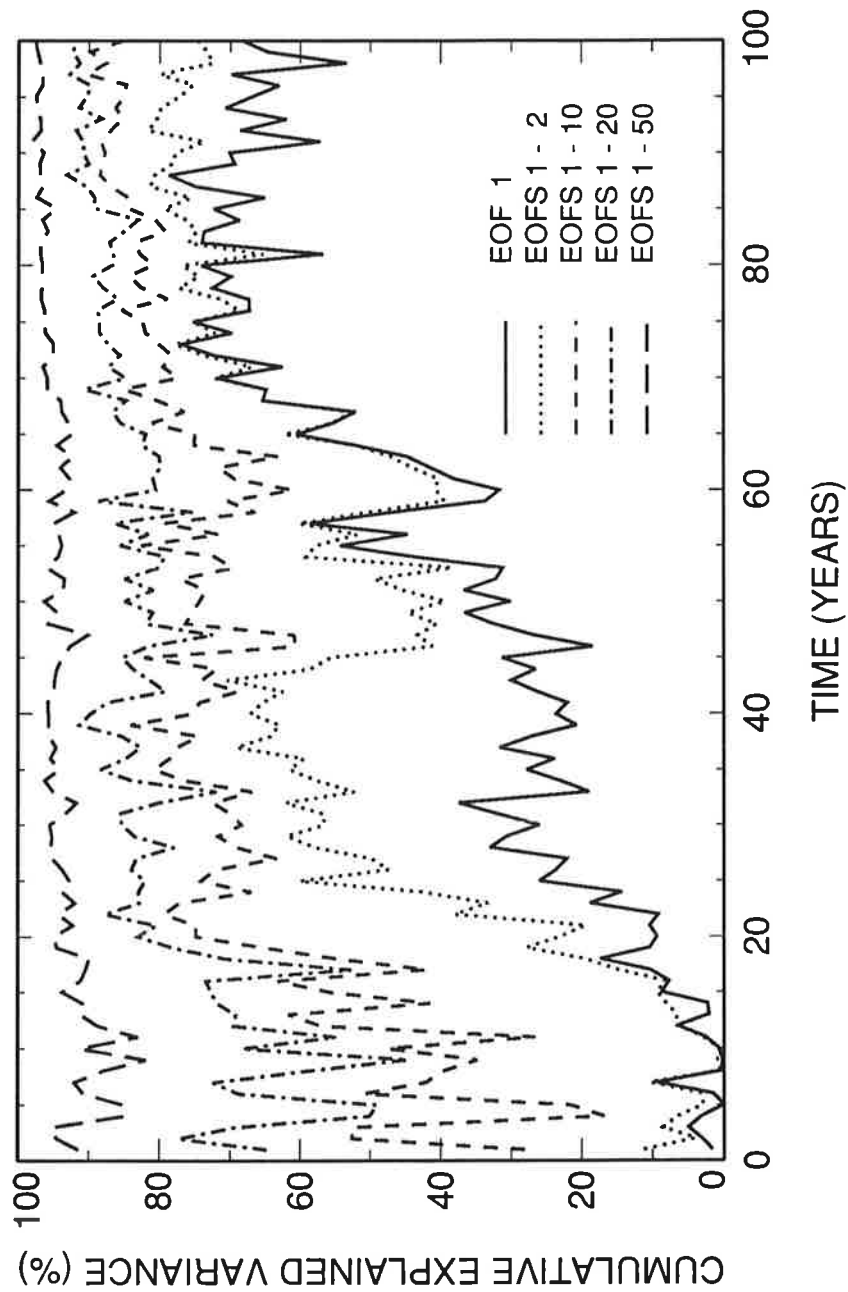


Figure 10c. Cumulative explained spatial variance of annually-averaged 2m temperature change (Definition 1) as a function of time and number of EOFs (1, 2, 10, 20, 50) for the control run.

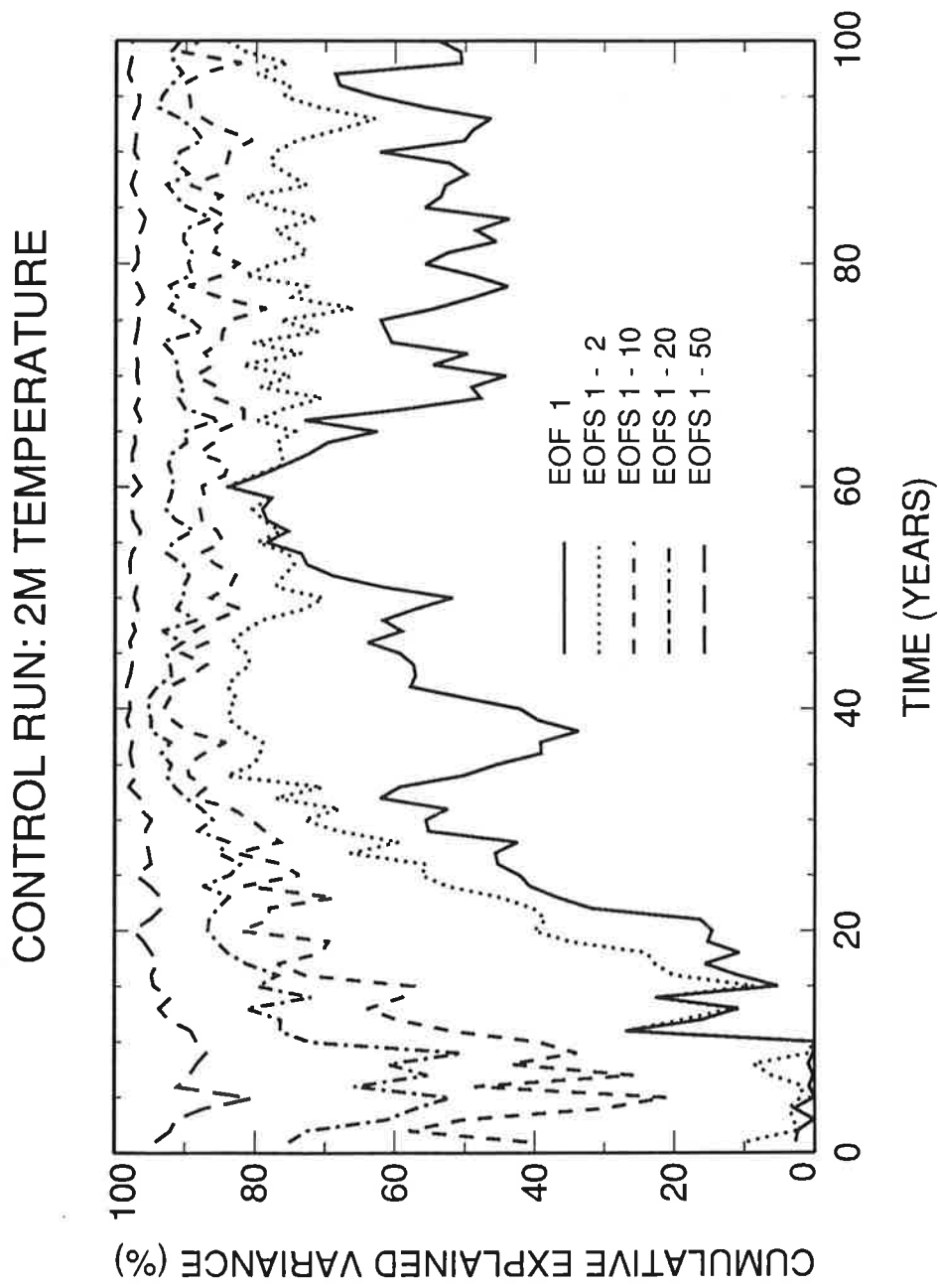
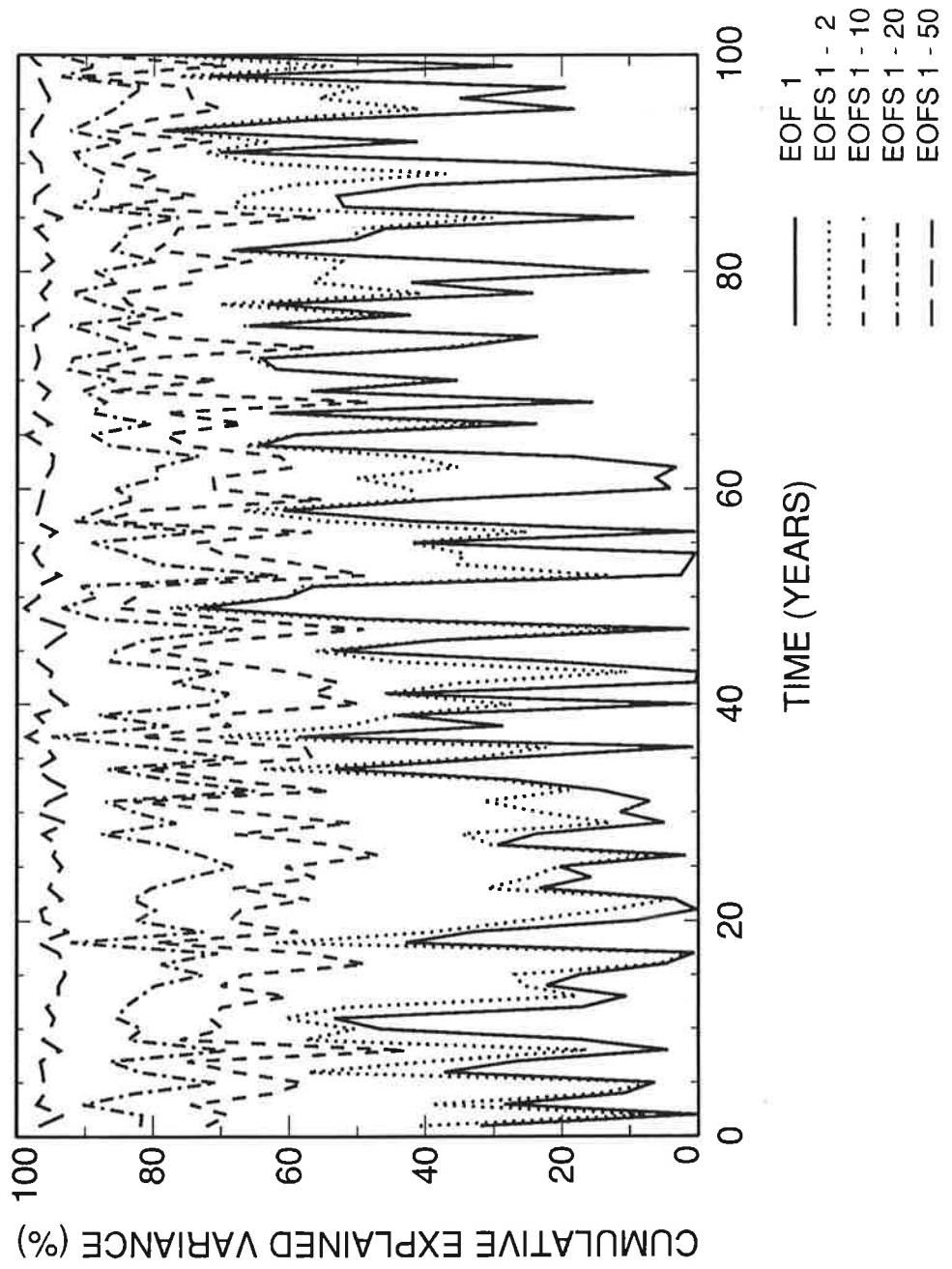
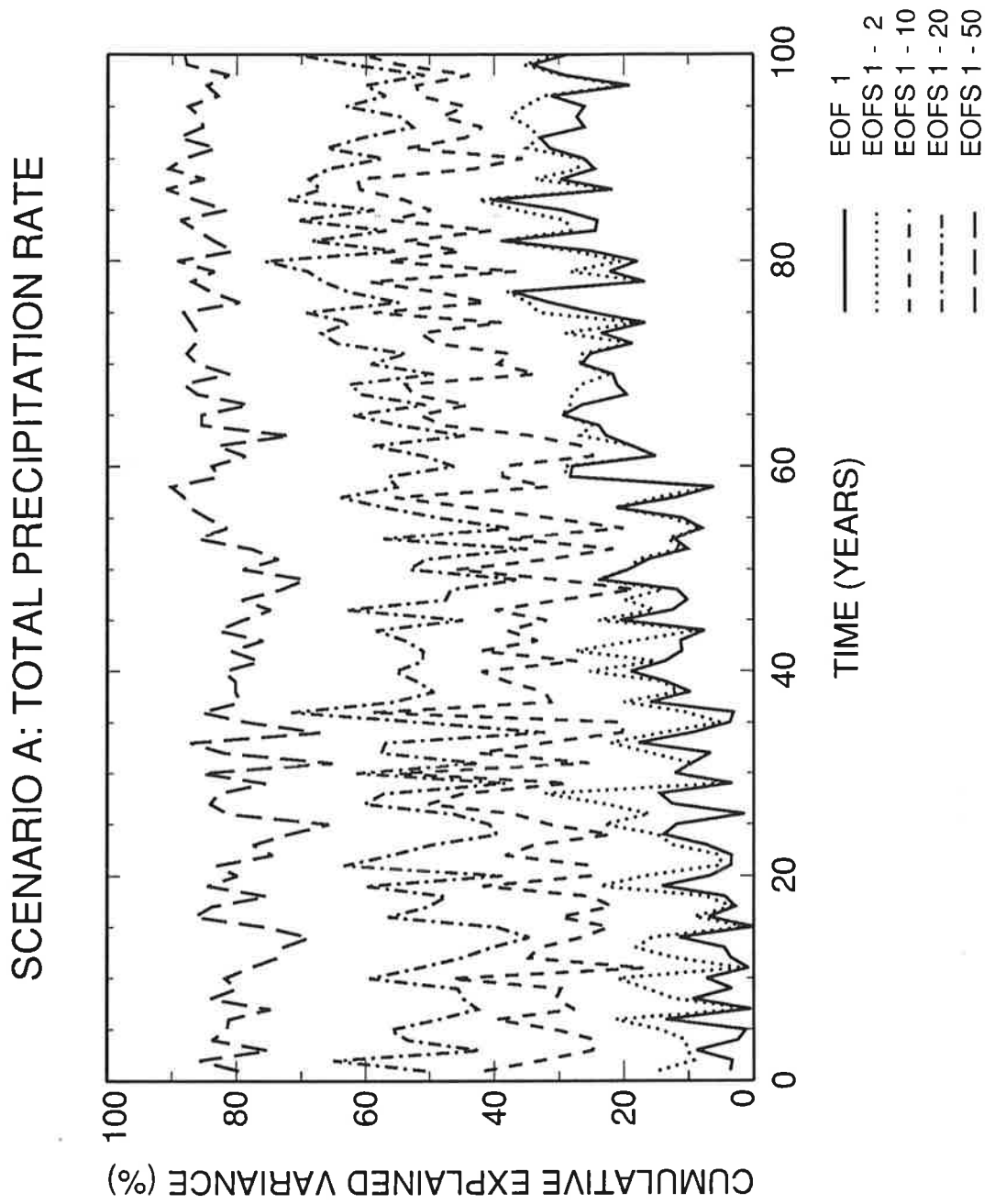


Figure 11a. Cumulative explained spatial variance for annually-averaged changes in sea-level pressure (Definition 1) in Scenario A as a function of time and number of EOFs (1, 2, 10, 20, 50).

### SCENARIO A: SLP



**Figure 11b.** Cumulative explained spatial variance for annually-averaged changes in total precipitation rate (Definition 1) in Scenario A as a function of time and number of EOFs (1, 2, 10, 20, 50).



**Figure 12a.** Principal component time series for the projection of the annually-averaged 2m temperature anomaly fields of the three greenhouse warming experiments and the control run onto EOF 1 of Scenario A. The control run data has a very small projection on EOF 1.

### 2M TEMP. DATA: PC TIME SERIES FOR PROJECTIONS ON SCENARIO A EOF 1

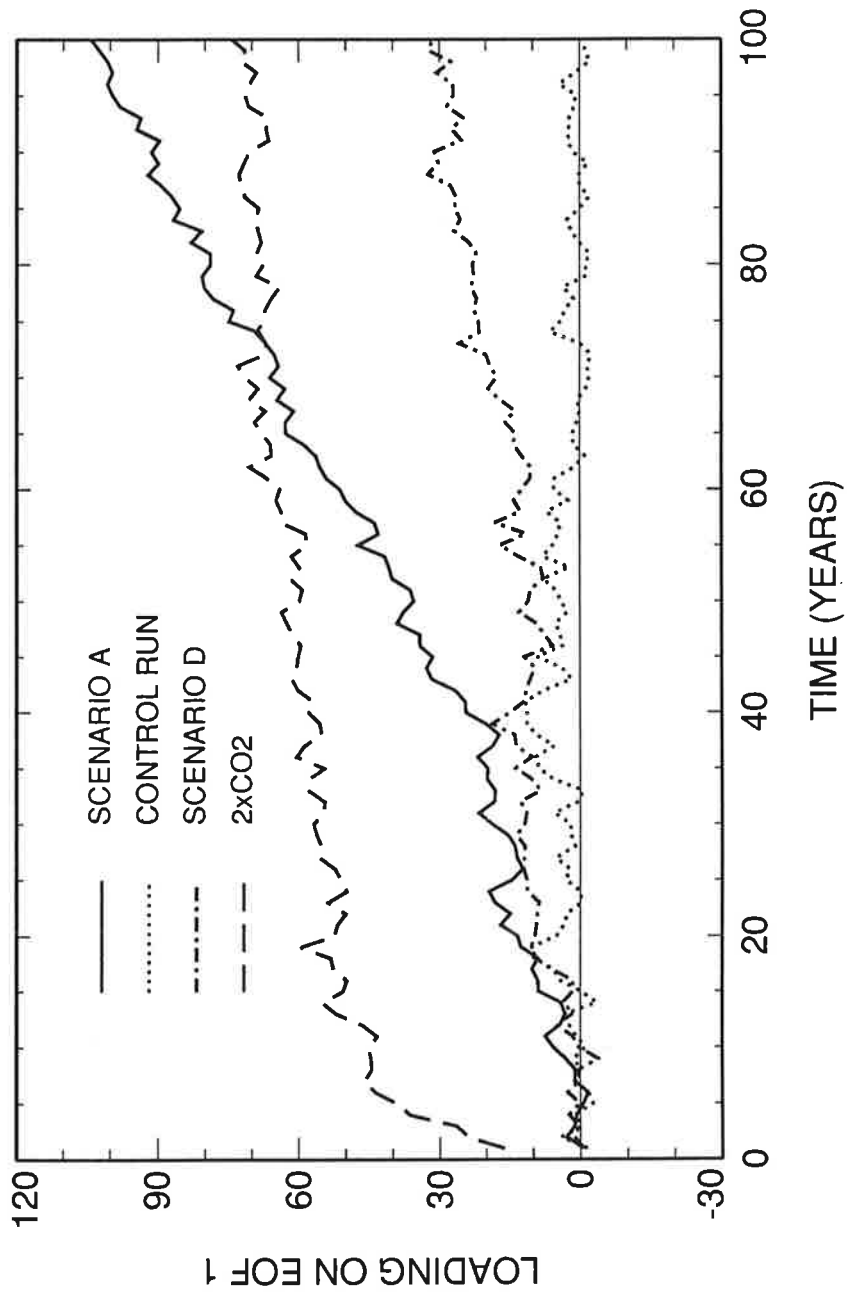


**Figure 12b.** Principal component time series for the projection of the annually-averaged 2m temperature anomaly fields of the three greenhouse warming experiments and the control run onto EOF 2 of Scenario A. The control run data has a large projection on EOF 2.

### 2M TEMP. DATA: PC TIME SERIES FOR PROJECTIONS ON SCENARIO A EOF 2

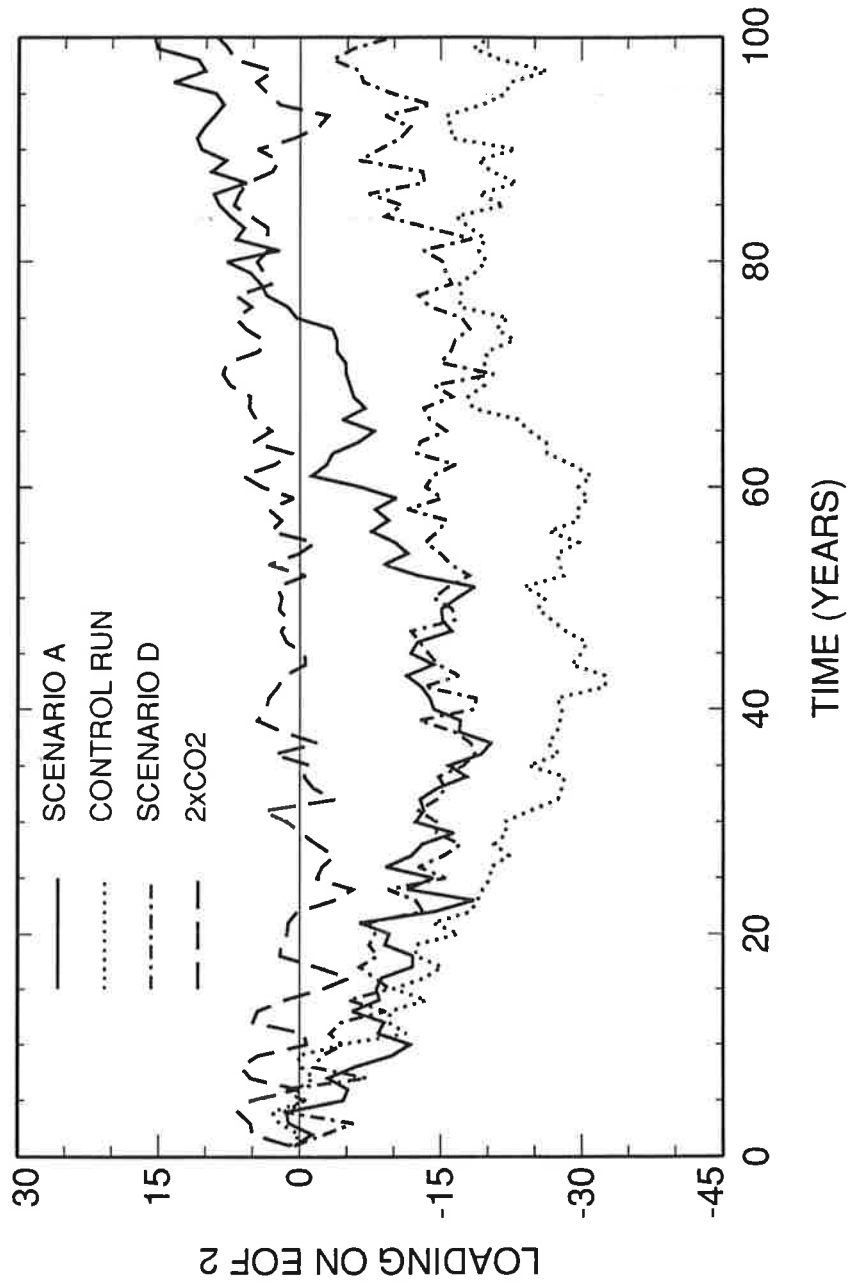


**Figure 13.** Principal component time series for the projection of the annually-averaged 2m temperature anomaly fields of the three greenhouse warming experiments and the control run onto EOF 1 of the control run. The amplitude of this pattern is large in Scenario D and in the first half of the Scenario A experiment.

### 2M TEMP. DATA: PC TIME SERIES FOR PROJECTIONS ON CONTROL EOF 1

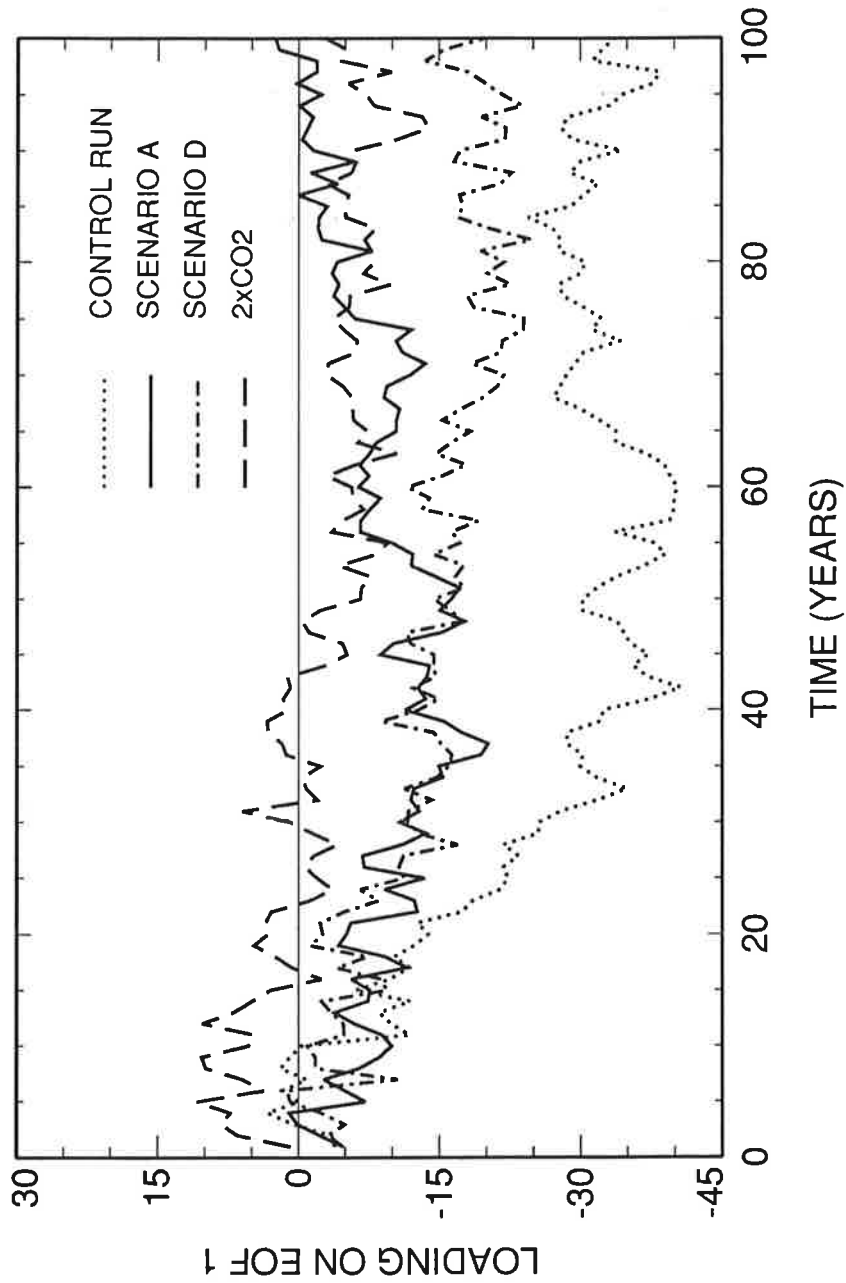


**Figure 14.** Principal component time series for the projection of the annually-averaged 2m temperature anomaly fields of the three greenhouse warming experiments and the control run onto the normalized land-sea mask of the ECHAM-1/LSG model. For both Scenario A and the 2xCO<sub>2</sub> experiment, approximately 28% of the total space-time variance of the anomaly data is explained by this projection.

### 2M TEMP. DATA: PC TIME SERIES FOR PROJECTION ON T21 LAND/SEA MASK

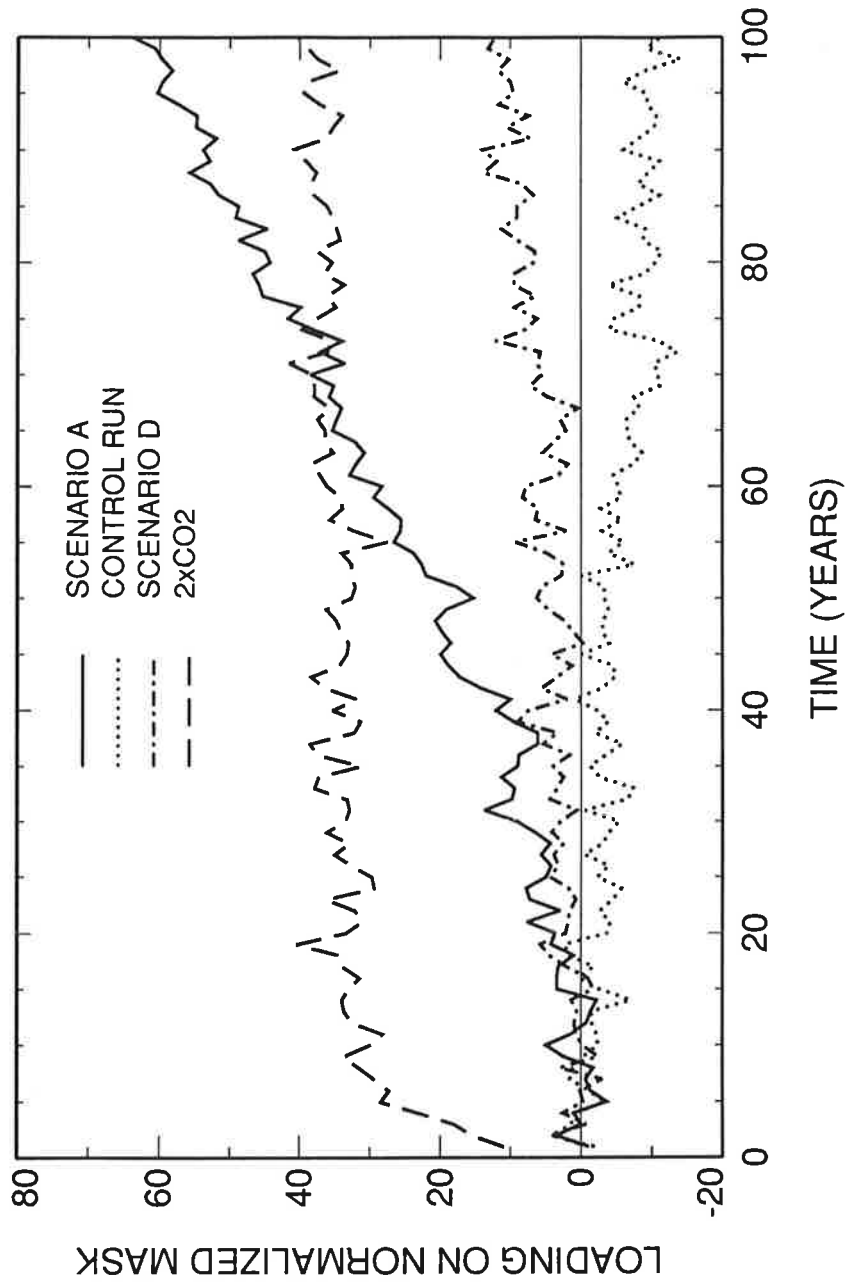


**Figure 15a.** Projection of the annually-averaged 2m temperature anomaly fields of the control run and Scenario A onto EOFs 1 and 2 of Scenario A. Each symbol represents one year of the control run or Scenario A, and the initial years of both experiments are marked. Note the divergent evolution of signal and noise.

### 2M TEMPERATURE DATA: PROJECTIONS ON SCENARIO A EOFs 1 + 2

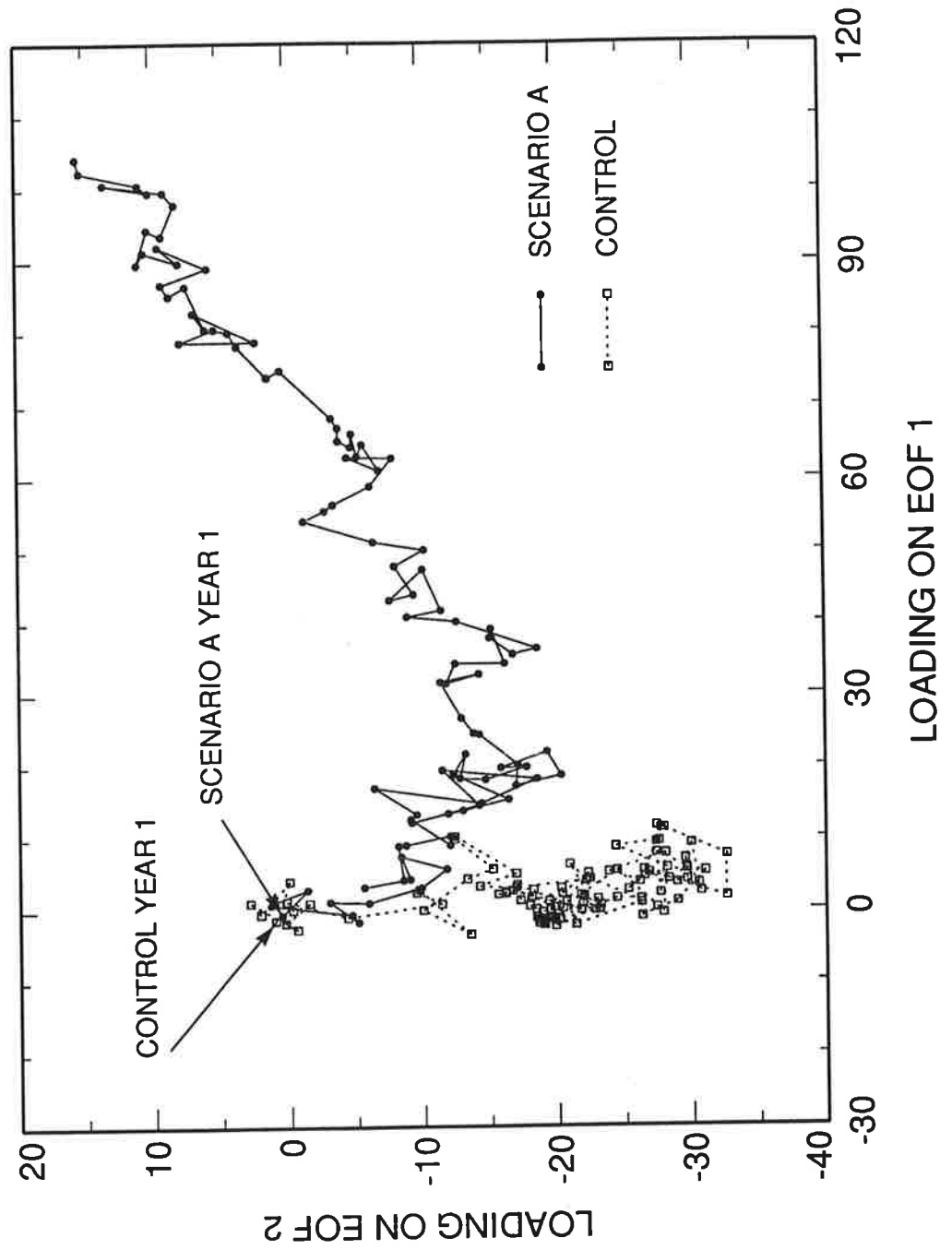


**Figure 15b.** Projection of the annually-averaged 2m temperature anomaly fields of the control run and Scenario A onto EOFs 2 and 3 of Scenario A. Each symbol represents one year of the control run or Scenario A, and the initial years of both experiments are marked. Note the overlap between the signal and noise clouds after the major component of the signal (EOF 1 of Scenario A; see figure 15a) has been removed.

### 2M TEMPERATURE DATA: PROJECTIONS ON SCENARIO A EOFS 2 + 3

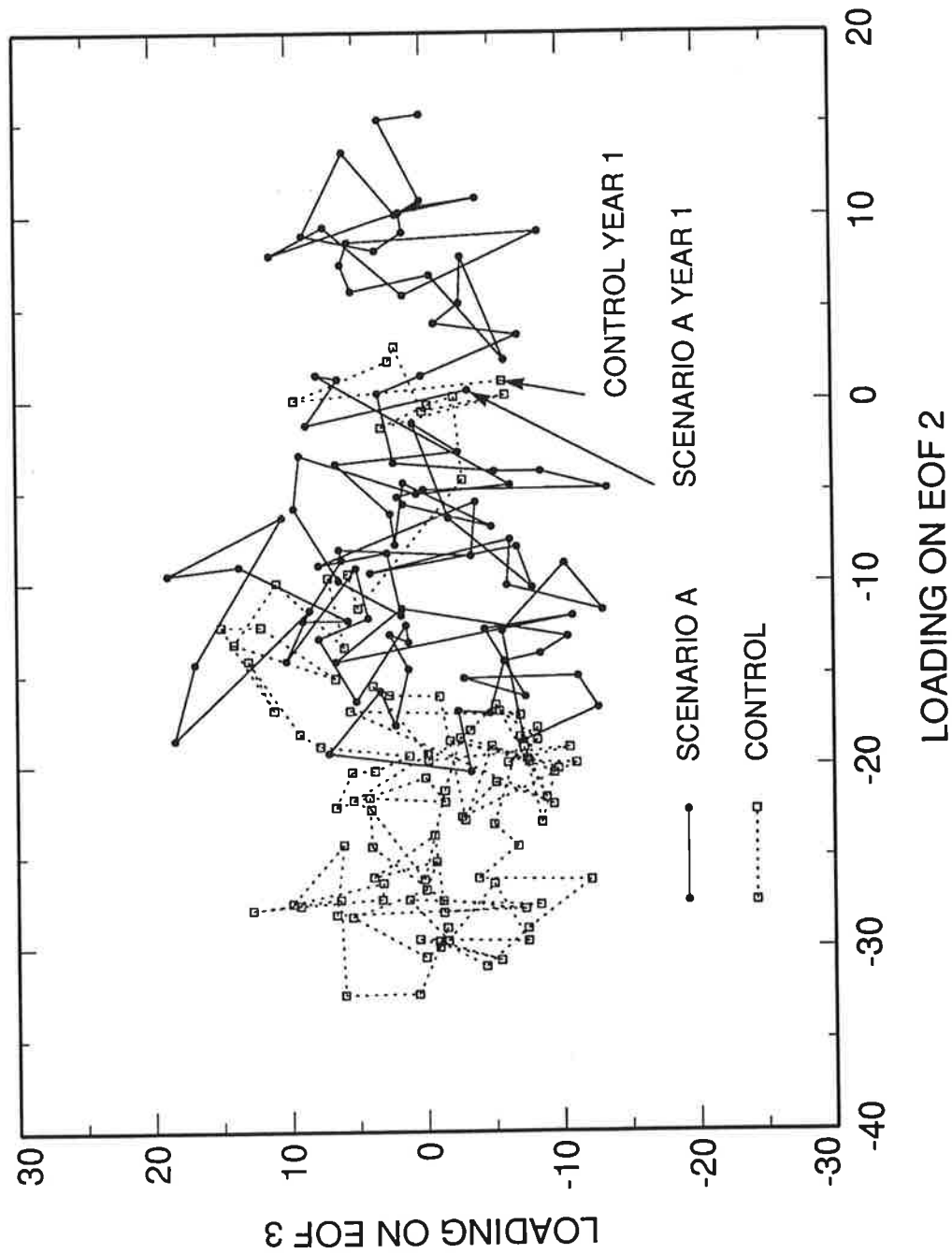


**Figure 16.** Projection of the annually-averaged 2m temperature anomaly fields of the control run and Scenario A onto EOFs 1 and 2 of the control run. Results are qualitatively similar to those in Figure 15a, indicating that the separation of signal and noise trajectories does not depend on the basis used for projection (Scenario A or control run EOFs).

**2M TEMPERATURE DATA: PROJECTIONS ON CONTROL EOFS 1 + 2**

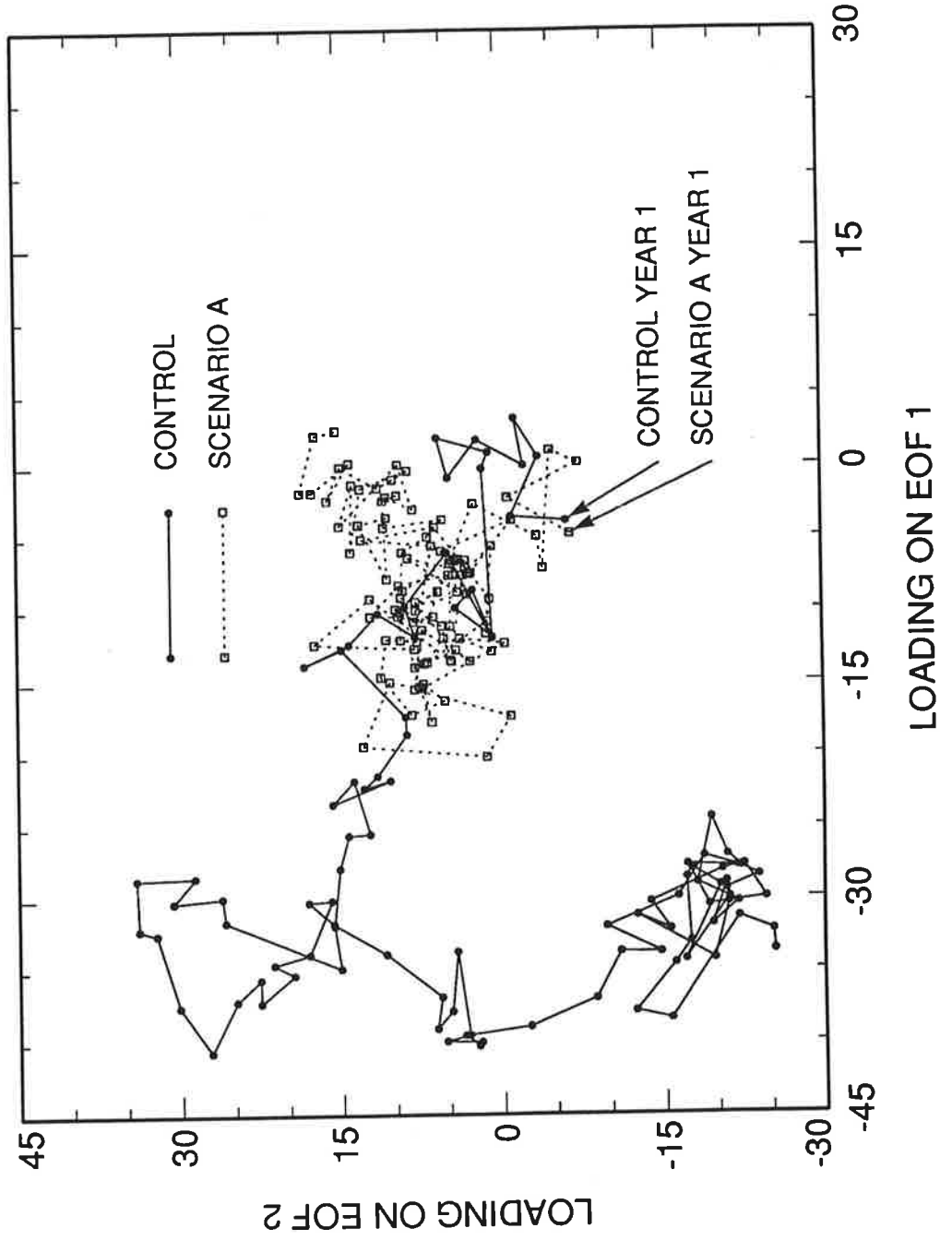
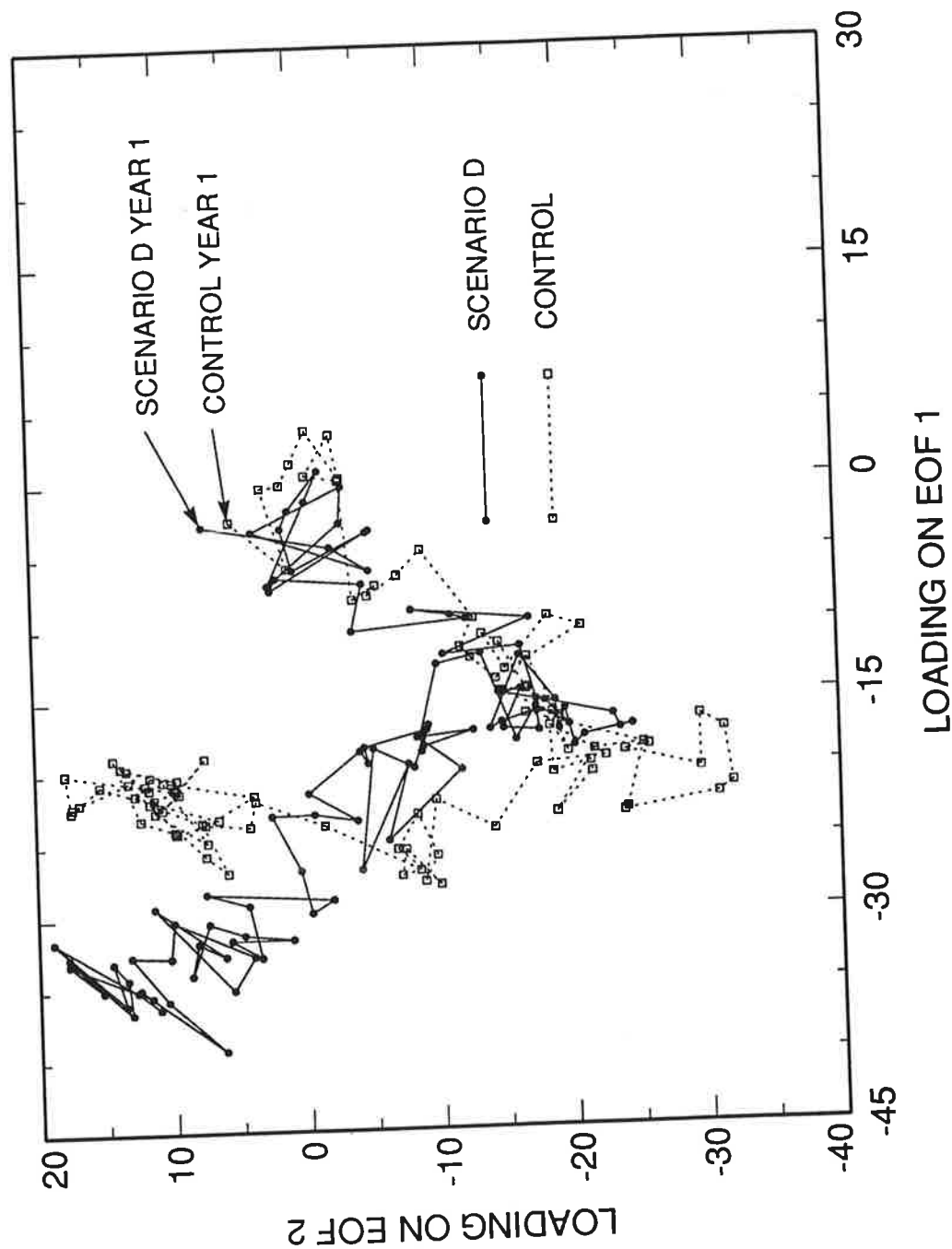


Figure 17. Projection of the annually-averaged 2m temperature anomaly fields of the control run and Scenario D onto EOFs 1 and 2 of Scenario D. Both integrations follow very similar trajectories for the first three to four decades.

## 2M TEMPERATURE DATA: PROJECTIONS ON SCENARIO D EOFs 1 + 2



**Figure 18.** Projection of the annually-averaged sea-level pressure anomaly fields of the control run and Scenario A onto EOFs 1 and 2 of Scenario A. There is considerable overlap between the clouds of signal and noise points in EOF space.

### SLP DATA: PROJECTIONS ON SCENARIO A EOFS 1 + 2

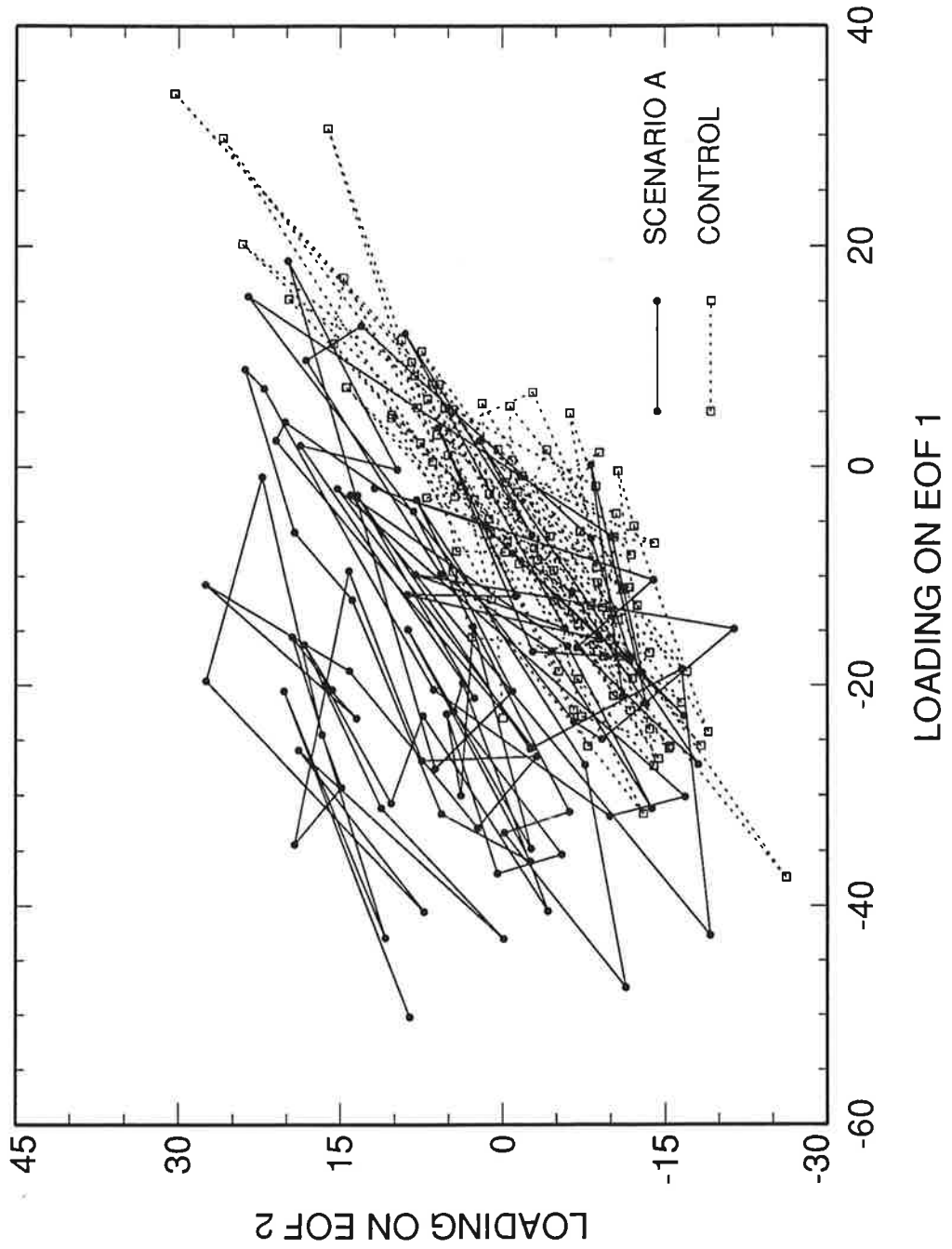


**Table 1.** Pattern correlations between EOF 1 of the control run and EOF 1 of the Scenario A experiment for 10 different climate variables. Results are for  $r$  (spatial means of EOF patterns subtracted) and  $r^*$  (spatial means included), and are ranked from smallest to largest value of  $r$ , i.e., in order of increasing similarity between dominant signal and noise patterns. All correlations are given as absolute values since the signs of the EOFs are not uniquely determined. Note that for 2m temperature,  $r^*$  is much smaller than  $r$ , since the Scenario A EOF 1 pattern is spatially coherent with a spatial mean nearly six times larger than that of the control run EOF 1 pattern. The explained variances of the control and Scenario A EOF 1 patterns are also given.

No.	Variable	Correlation		Explained Variance	
		$r$	$r^*$	CTL (%)	SZA (%)
1	Vertical U-Velocity	0.29	0.36	23.6	80.5
2	2 m Temperature	0.43	0.09	52.5	84.1
3	Vertical Temperature	0.46	0.57	61.4	97.6
4	Precipitable Water	0.50	0.65	27.7	89.5
5	Precipitation Rate	0.55	0.51	12.8	17.3
6	Total Cloud Cover	0.57	0.57	16.1	22.4
7	10 m U-Velocity	0.67	0.66	17.4	28.4
8	10 m V-Velocity	0.69	0.70	20.1	25.9
9	Vertical V-Velocity	0.72	0.73	29.5	56.3
10	Sea Level Pressure	0.82	0.80	27.7	36.9

**Table 2.** Pattern correlation matrix for EOFs 1 and 2 of Scenarios A, D, 2xCO<sub>2</sub> and control run. All EOFs were computed using annually-averaged 2 m temperature data. Pattern correlations were calculated with spatial means of EOF patterns subtracted ( $r$ ) and with spatial means included ( $r^*$ ). For clarity, values of  $r^*$  are in bold font. All correlations are given as absolute values since the signs of the EOFs are not uniquely determined.

EXP	EOF	EV(%) <sup>1</sup>	EOF 1					EOF 2										
			SZA <sup>2</sup>		SZD <sup>3</sup>		TCO <sup>4</sup>		CTL <sup>5</sup>		SZA		SZD		TCO		CTL	
			$r$	$r^*$	$r$	$r^*$	$r$	$r^*$	$r$	$r^*$	$r$	$r^*$	$r$	$r^*$	$r$	$r^*$	$r$	$r^*$
SZA	1	84.1	1.00	<b>1.00</b>	0.82	<b>0.74</b>	0.97	<b>0.99</b>	0.43	<b>0.09</b>	0.30	<b>0.00</b>	0.22	<b>0.05</b>	0.33	<b>0.00</b>	0.35	<b>0.14</b>
SZD	1	46.8			1.00	<b>1.00</b>	0.75	<b>0.71</b>	0.81	<b>0.66</b>	0.65	<b>0.51</b>	0.03	<b>0.00</b>	0.38	<b>0.25</b>	0.26	<b>0.07</b>
TCO	1	87.8					1.00	<b>1.00</b>	0.35	<b>0.05</b>	0.22	<b>0.04</b>	0.65	<b>0.05</b>	0.34	<b>0.00</b>	0.31	<b>0.16</b>
CTL	1	52.5							1.00	<b>1.00</b>	0.74	<b>0.75</b>	0.16	<b>0.15</b>	0.37	<b>0.39</b>	0.06	<b>0.00</b>
SZA	2	3.1									1.00	<b>1.00</b>	0.47	<b>0.45</b>	0.14	<b>0.10</b>	0.24	<b>0.16</b>
SZD	2	12.4											1.00	<b>1.00</b>	0.65	<b>0.65</b>	0.86	<b>0.82</b>
TCO	2	2.7													1.00	<b>1.00</b>	0.59	<b>0.61</b>
CTL	2	18.6															1.00	<b>1.00</b>

<sup>1</sup> EV: Explained variance.

<sup>2</sup> SZA: Scenario A.

<sup>3</sup> SZD: Scenario D.

<sup>4</sup> TCO: 2xCO<sub>2</sub>.

<sup>5</sup> CTL: Control.

**Table 3.** Explained variance for projection of control run data onto Scenario A EOFs, and Scenario A data onto control run EOFs. Results are for  $k_c$ , the number of control run EOFs required in order to explain 95% of the control run variance, and  $k_s$ , the number of Scenario A EOFs required to explain 95% of the Scenario A variance.  $V_q^{sc}$  and  $V_q^{cs}$  are (respectively) measures of how well the Scenario A data can be represented in the truncated space of the first 99 control EOFs and how well the control run data can be represented in the truncated space of the first 99 Scenario A EOFs.  $V_1^{sc}$ ,  $V_1^{cs}$ ,  $V_2^{sc}$  and  $V_2^{cs}$  are analogous to  $V_q^{sc}$  and  $V_q^{cs}$ , but now the projections are restricted to the EOF 1 and EOF 2 patterns of the control run and Scenario A. For further details, refer to Section 4.2.

No.	Variable	$k_c^1$	$k_s^2$	$V_q^{sc^3}$	$V_q^{cs^4}$	$V_1^{sc^5}$	$V_1^{cs^6}$	$V_2^{sc^7}$	$V_2^{cs^8}$
1	Vertical Temperature	24	1	89.1	96.6	31.5	20.6	2.5	18.4
2	Vertical U-Velocity	24	9	98.2	98.9	13.3	9.4	28.0	18.7
3	Vertical V-Velocity	35	27	93.1	94.1	30.7	17.2	8.8	6.6
4	Sea Level Pressure	48	44	82.0	86.5	26.8	18.3	4.4	9.4
5	Total Cloud Cover	84	84	32.4	32.8	8.7	5.4	0.4	5.7
6	10 m U-Velocity	64	62	73.7	73.3	14.6	10.6	7.9	6.5
7	10 m V-Velocity	70	69	64.6	64.4	13.9	10.4	3.5	6.6
8	2 m Temperature	40	19	66.4	81.8	2.6	1.2	2.1	30.2
9	Precipitable Water	75	21	78.1	57.5	37.7	12.3	0.3	10.5
10	Precipitation Rate	80	80	43.0	45.0	6.5	3.9	2.1	5.5

<sup>1</sup> Number of control run EOFs required in order to explain  $\geq 95\%$  of the total control run variance.

<sup>2</sup> Number of Scenario A EOFs required in order to explain  $\geq 95\%$  of the total Scenario A variance.

<sup>3</sup> Percentage of total Scenario A space-time variance explained by projection of Scenario A anomaly data onto first 99 control run EOFs.

<sup>4</sup> Percentage of total control run space-time variance explained by projection of control run anomaly data onto first 99 Scenario A EOFs.

<sup>5</sup> Percentage of total Scenario A space-time variance explained by projection of Scenario A anomaly data onto EOF 1 of control run.

<sup>6</sup> Percentage of total control run space-time variance explained by projection of control run anomaly data onto EOF 1 of Scenario A.

<sup>7</sup> Percentage of total Scenario A space-time variance explained by projection of Scenario A anomaly data onto EOF 2 of control run.

<sup>8</sup> Percentage of total control run space-time variance explained by projection of control run anomaly data onto EOF 2 of Scenario A.